Diploma thesis

Investigation of water absorption of cellulose fibers by gravimetric analysis and atomic force microscopy

by
Patrice Kreiml

at the Institute of Physics
Montanuniversität Leoben, Austria

under supervision of
Ao. Univ. Prof. Dr. Christian Teichert
Dipl.-Ing. Dr. Christian Ganser

refereed by
Ao. Univ. Prof. Dr. Christian Teichert

Leoben, Februar 2016

dedicated to my family

Eidesstattliche Erklärung

Ich erkläre an Eides statt, dass ich diese Arbeit selbständig verfasst, andere als die angegebenen Quellen und Hilfsmittel nicht benutzt und mich auch sonst keiner unerlaubten Hilfsmittel bedient habe.

Affidavit

I declare in lieu of oath, that I wrote this thesis and performed the associated research myself, using only literature cited in this volume.

Patrice Kreiml
Leoben, Februar 2016

Abstract

Cellulose fibers are the base for a variety of products in our daily lives, such as paper, construction, textile, hygiene, and medical products. For several of these products, the native cellulose fibers, extracted from wood, are insufficient. Textile, hygiene, and medical products require long fibers, that can be spun into a thread. In the viscose process, native cellulose fibers from pulp are dissolved in a viscose solution and spun into pure viscose fibers.

This work is divided into two parts. One part comprises the measurement of water absorption of cellulosic fibers by employing a sorption balance. The term sorption denotes absorption, as well as desorption. The sorption balance in this work recorded the gravimetric uptake and decrease of water vapor at varying water vapor pressure at 17 °C. The obtained sorption isotherms were also used to determine the absorption behavior of the fibers. The samples for the sorption measurements were provided by an industrial collaborator. The samples consisted of three different types of viscose fibers, called Bellini, Verdi, and Danufil, as well as a sample of pulp fibers from a mixture of spruce and pine. Two configurations of sample preparations were employed, one with loose bundles of fibers, and the other one with tightly packed fibers compressed into a wire whisk. In the former, single fiber properties were measured, and the relative water absorption of the different types of viscose fibers was very similar. All viscose fiber samples exhibited a relative water absorption slightly above 20 % and the pulp fiber sample slightly below 20 %. The compressed viscose samples yielded a relative water absorption above 30 %, whereas for the compressed pulp samples it was 26 %. The higher values are thought to be caused by network effects of the tightly packed samples, which is supported by the shape of the isotherms.

The other part of this thesis was dedicated to the investigation of viscose fiber surfaces with atomic force microscopy (AFM). The investigated samples comprised two sets of trilobal viscose fibers provided by an industrial supplier. Each set consisted of two batches from the same production line, one set with water absorption capacity above average and the other one with values below average. Under the assumption that the fibers' surfaces contribute significantly to the water uptake, AFM was employed to find a correlation between water uptake and surface features. The analysis of the three roughness parameters RMS-roughness σ, lateral correlation length ξ, and Hurst parameter α yielded no correlation to water absorption. Trenches covering all fiber surfaces were analyzed thoroughly regarding their angle, length, and density. In the end, only the trench density in both sample sets exhibited a possible correlation, where a lower trench density correlated to higher water absorption.

Kurzfassung

Zellulosefasern bilden die Basis für eine Vielzahl von Produkten in unserem täglichen Leben, wie Papier-, Bau- , Textil-, Hygiene- und medizinische Produkte. Für einige dieser Produkte sind die natürlichen Fasern, die aus Holz gewonnen werden, unzureichend. Textilien, Hygiene- und medizinische Produkte erfordern lange Fasern, die zu Fäden gesponnen werden können. Im Viskoseprozess werden natürliche Zellulosefasern aus dem Zellstoff in einer viskosen Lösung aufgelöst und in reine Viskosefasern gesponnen.

Diese Arbeit ist in zwei Teile aufgeteilt. Ein Teil stellt die Messung der Wasserabsorption von zellulosischen Fasern unter Verwendung einer Sorptionswaage dar. Der Term Sorption bezeichnet Absorption wie auch Desorption. Die Sorptionswaage in dieser Arbeit nimmt die gravimetrische Aufnahme und Abnahme von Wasserdampf bei sich ändernden Wasserdampfdrücken bei 17 °C auf. Die erhaltenen Sorptionsisothermen wurden auch zur Bestimmung des Absorptionsverhaltens der Fasern genutzt. Die Proben für die Sorptionsmessungen wurden von einem industriellen Kooperationspartner bereitgestellt. Die Proben bestanden aus drei verschiedenen Typen von Viskosefasern, namens Bellini, Verdi und Danufil sowie einer Probe von Zellstofffasern, bestehend aus einer Mischung aus Fichte und Kiefer. Zwei Anordnungen der Probenvorbereitung wurden verwendet, eine mit losen Faserbündeln und eine andere mit dicht gepackten Fasern, die in einem Drahtgeflecht komprimiert wurden. In erst genannter Anordnung wurde Einzelfaserverhalten gemessen, und die relative Wasserabsorption der veschiedenen Viskosefasern war sehr ähnlich. Alle Viskosefaserproben wiesen eine relative Wasserabsorption von etwas über 20 % und die Zellstofffaserprobe eine von etwas unter 20 % auf. Die verdichteten Viskosefasern erreichten eine relative Wasserabsorption von über 30 %, während die verdichteten Zellstofffasern 26 % erreichten. Die höheren Werte der verdichteten Proben werden Netzwerkeffekten zugeschrieben, was von der Form der Isothermen unterstützt wird.

Der andere Teil dieser Arbeit beschäftigte sich mit der Untersuchung von Viskosefaseroberflächen mittels Rasterkraftmikroskop (AFM). Die untersuchten Proben bestanden aus zwei Garnituren von trilobalen Viskosefasern, die vom industriellen Zulieferer stammten. Jede Garnitur bestand aus zwei Sätzen von derselben Produktionslinie, wobei ein Satz eine überdurchschnittliche und der andere eine unterdurchschnittliche Wasseraufnahmefähigkeit aufwies. Unter der Annahme, dass die Faseroberflächen einen wesentlichen Beitrag zur Wasseraufnahme beisteuern, wurde das AFM eingesetzt, um eine Beziehung zwischen Wasseraufnahme und Oberflächeneigenschaften zu finden. Die Analyse der drei Rauigkeitsparameter RMS-Rauigkeit σ, laterale Korrelationslänge ξ und Hurstparameter α lieferten keine Beziehung zu Wasserabsorption. Gräben, welche alle Faseroberflächen bedecken, wurden gründlich in Bezug auf ihre Winkel, Länge und Dichte untersucht. Schlussendlich zeigte nur die Gräbendichte in beiden Probengarni-

turen eine mögliche Beziehung, in der eine niedrige Gräbendichte mit einer höheren Wasserabsorption korreliert.

Acronyms

σ	Root mean square (RMS) roughness
ξ	Lateral correlation length
α	Hurst parameter
f_r	Resonance frequency
1D	One-dimensional
2D	Two-dimensional
3D	Three-dimensional
AFM	Atomic force microscopy
FFT	Fast Fourier transform
HHCF	Height-height correlation function
L	Lumen
ML	Middle lamella
N_t	Number of trenches
OM	Optical micrograph
P	Primary wall
RH	Relative humidity (φ_r)
S1	Secondary wall number one
S2	Secondary wall number two
S3	Secondary wall number three
SEM	Scanning Electron Microscopy
T	Temperature

Contents

1 Motivation

It has been well over 100 years since two British chemists discovered a method to dissolve wood cellulose as cellulose xanthogenate [1,2]. This discovery lead to the method, which is known today as the viscose process. In the viscose process, pulp is dissolved in aqueous NaOH as a xanthogenate derivative. After wet spinning in sulfuric acid, pure viscose fibers are produced. Today, the viscose process has an annual world production of about 2.2 million tons (2002) [3]. Viscose fibers have a wide range of use, among them textile, hygiene, and medical applications are prominent. For aforementioned applications, water absorption plays a vital role.

One of the two main topics of this work is the determination of the relative water absorption of different types of viscose fibers in comparison to pulp fibers. Therefore, a sorption balance was employed, which records the gravimetric water uptake and decrease versus a continuously changed relative humidity (RH) at constant temperature. The obtained data can be graphically displayed as a sorption isotherm. The interpretation of the isotherms yields information about the composition of the sample. The reason for this measurements was to compare the water absorption behavior of the different fibers and additionally to draw conclusions about the interior of the fibers and influences on their water uptake.

The other part of this work is dedicated to the surfaces of viscose fibers. There, the topography and morphology of the fiber surfaces was investigated. The goal was to find references on surface features influencing water absorption. This was realized by the employment of atomic force microscopy (AFM). The samples are viscose fibers from the same production line, where different batches display different capabilities of water uptake. For equalization and in order to maintain an unchanging quality of the commercial product, fibers from various batches with different water absorption capabilities are mixed. This generates costs for storage and additional effort. By detecting and directing the factors influencing water absorption, the production process can be better controlled and thus, reduce costs.

2 Theoretical background

2.1 Cellulose fibers

Cellulose is a polysaccharide composed of D-glucopyranose units. Fig. 2.1 shows a structural representation of a cellulose molecule. After extracting the cellulose from wood, the obtained fibers are referred to as native cellulose fibers or pulp fibers. Like many polymers, cellulose is able to form crystalline regions between the amorphous areas. In these fibers, cellulose crystallizes as cellulose type I with an amount of crystalline regions of up to 65 %. [4]. The native cellulose fibers can be refined to man-made or regenerated fibers. Among them are viscose fibers with the crystalline structure cellulose II. In this work, pulp fibers and viscose fibers were investigated. In the following, the raw materials wood, pulp, and viscose fibers will be discussed.

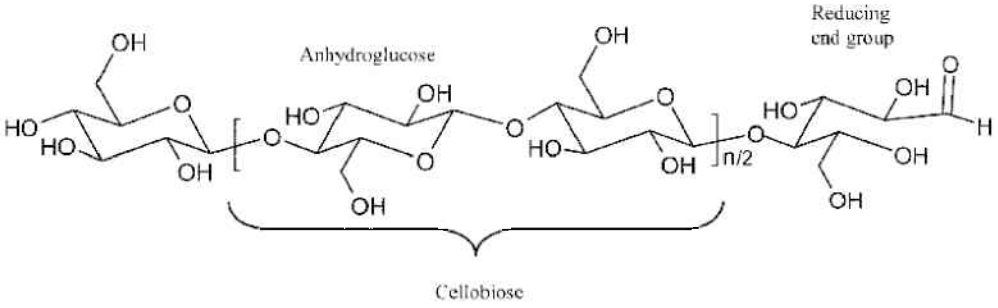

Figure 2.1: Structural formula of a cellulose molecule. Within the brackets is the repeating base unit. From [5].

2.1.1 Wood

Wood is a hierarchical structured, natural grown compound. A scheme of the hierarchical structure of a conifer tracheid is sketched in Fig. 2.2. The main components of wood are cellulose, hemicellulose, and lignin.

The smallest unit in wood is the cellulose molecule, which measures only a few Ångström in diameter. These molecules form elementary fibrils. These elementary fibrils are located in the cell walls and are <10 nm in diameter. On the next hierarchical level, they form microfibrils with 10 nm - 60 nm in diameter [6,7]. Lignin and hemicellulose are located between the elementary and microfibrils and serve as an intermediate. It is assumed that lignin and hemicellulose act as glue that adds to the stiffness of the wood [8,9].

In the center of a wood cell is a void called the lumen (L). The lumen is used for water transport in the tree. A thick cell wall consisting of several layers winds helically, but with different preferential orientations of the microfibrils, around L. The outermost layer is the primary layer (P). From P to L the layers are called secondary layers one to three (S1, S2, S3). There, microfibrils are highly oriented, while the the microfibrils in P are disordered. S2 as the thickest layer, determines the mechanical properties of the cell. The middle lamella (ML) is located between the cells and is rich in lignin.

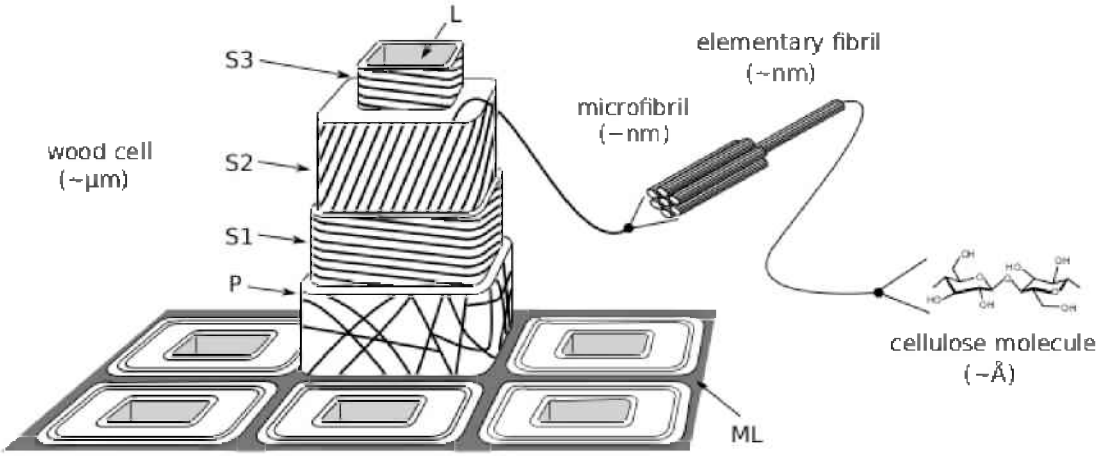

Figure 2.2: The hierarchical structure of wood from the wood cell to a single cellulose molecule. The characteristic length scales of the respective hierarchy levels can be found by the length units given in brackets [10].

2.1.2 Pulp fibers

For the production of paper or viscose fibers, however, the wood cells have to be extracted from the wood. At this point the extracted wood cells are generally referred to as pulp fibers. The extraction of the wood cells can be achieved by mechanical and/or chemical methods. The freed wood cells reside in an aqueous suspension. Additionally, lignin and hemicellulose are removed from the wood. From here, a further refining process can be added. Refining of pulp fibers is a mechanical treatment. In a mill, shear stress is applied on the pulp fibers and results in highly conformable fibers with loose microfibrils dangling from the fiber. These dangling microfibrils have a beneficial effect in paper production [11].

2.1.3 Viscose fibers

Today, there are several methods to extract cellulose from pulp fibers and to spin it into regenerated fibers, e.g. viscose, modal, and lyocell processes [3,12]. In the viscose process, pulp is swollen in a sodium hydroxide (NaOH) bath. After treating the swollen pulp with carbon disulfide (CS_2), a cellulose xanthogenate is generated. The

CS_2 derivative is soluble in aqueous NaOH and yields a viscous solution. Then, in the process of wet spinning in aqueous sulfuric acid (H_2SO_4), pure insoluble viscose fibers are produced. The CS_2 separates from the viscose, while NaOH and H_2SO_4 neutralize each other [13].

The cross-section of the viscose fiber is determined by the shape of the spinneret. Fig. 2.3 reveals scanning electron microscope (SEM) images of viscose fibers with different cross-sections. The length of the viscose fibers can be simply adjusted by cutting them into the desired length.

The crystalline structure in viscose fibers (cellulose II) is different from the crystalline structure of pulp fibers (cellulose I). Cellulose II is believed to be thermodynamically more stable [3]. In viscose fibers, the amount of crystalline cellulose II is mostly reported to be between 30 % and 50 % [3,14,15]. One of the advantages of viscose fibers is their length compared to pulp fibers. Viscose fibers can be formed to long threads. This simplifies manufacturing for applications like textiles, hygiene products, money bills, and special papers.

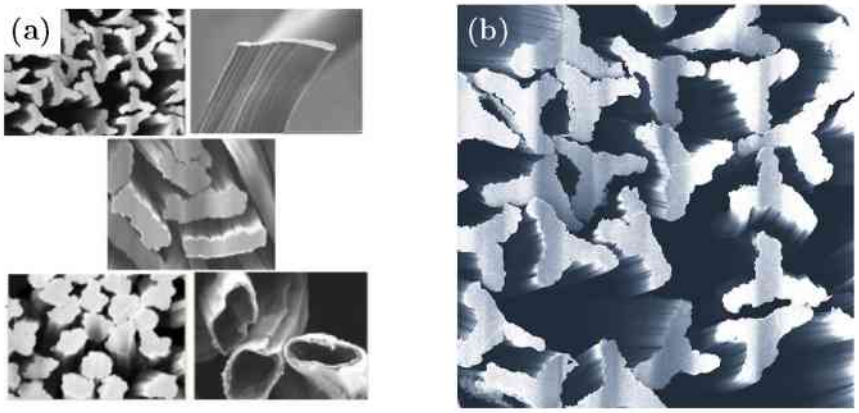

Figure 2.3: Scanning electron microscope (SEM) images of various viscose fiber cross-sections in (a) [16]. (b) shows a more detailed image of a trilobal viscose fiber [17].

2.2 Sorption measurements

The sorption measurements presented in this work are in principle gravimetric measurements. By regulating the relative humidity (RH), the mass change Δm caused by isothermal water vapor uptake and release is recorded.

2.2.1 Relative humidity

The relative humidity is a very important parameter in sorption measurements and is defined as

$$RH = \frac{p_{H_2O}}{p^*_{H_2O}(\vartheta)}. \tag{2.1}$$

RH is a ratio of the partial water vapor pressure p_{H_2O} to the saturation water vapor pressure $p^*_{H_2O}(\vartheta)$, which depends on temperature ϑ. This dependency of $p^*_{H_2O}(\vartheta)$ on ϑ is given by the relation

$$p^*_{H_2O}(\vartheta) = \alpha \cdot exp\left(\frac{\beta\vartheta}{\lambda + \vartheta}\right), \tag{2.2}$$

with ϑ in °C, empirically determined constants $\alpha = 6.122$ hPa, $\beta = 17.62$, and $\lambda = 243.12$ °C [18]. With increasing temperature, the maximum amount of gaseous water in air increases strongly, as is illustrated in Fig. 2.4a. On the other hand, with decreasing temperature and p_{H_2O} remaining constant, condensation will occur when $p^*_{H_2O}(\vartheta) = p_{H_2O}$, where $RH = 1$, as indicated in Fig. 2.4b.

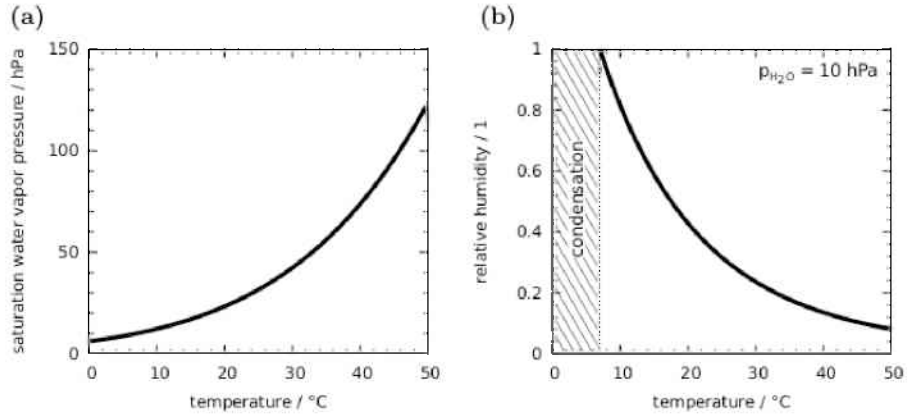

Figure 2.4: Temperature dependency of (a) the saturation water vapor pressure $p^*_{H_2O}(\vartheta)$ and (b) the relative humidity. In (b), at $\vartheta < 7$°C, condensation occurs [10].

2.2.2 Analysis of the sorption curves

Sorption measurements are divided into adsorption and desorption. Adsorption is the attachment of an atom, ion or molecule on a surface. Between the surface (adsorbent) and the adsorbable gas (adsorptive) is an interfacial layer, which is compromised of two regions. One is the surface layer of the adsorbent and the other is the adsorption space in which enrichment of the adsorptive can occur. Once a particle from the adsorption space is attached to the surface, the adsorptive is referred to as adsorbate. Desorption is actually the reversed process to adsorption, in which the adsorbed amount decreases. The term absorption is used, when the adsorptive penetrates the surface layer and enters the bulk solid. The differentiation of adsorption and absorption is sometimes

difficult, impossible or even irrelevant. Thus, the wider term sorption and the derived terms sorbent, sorptive, and sorbate will be used.

An issue - when analyzing sorption curves - is the distinction between external and internal (e.g. pores) surface in porous materials. Since the surface of most materials is rough rather than atomically smooth, not only the matter of external and internal surface is obscure, even adsorption and absorption is hard to determine. There are conventions, but the demarcation depends on the methods of assessment and on the type of pores and their size distribution. In practice, the accessibility of pores may depend on the dimensions of the sorptive (molecular sieve effect [19]) or the roughness of the surface. To avoid ambiguities when pores are discussed, this work adheres to the IUPAC (International Union of Pure and Applied Chemistry) classification, which is presented in table 2.1.

Table 2.1: Classification of pores according to their sizes by IUPAC.

type	size
micropores	d < 2 nm
mesopores	2 mm < d < 50 nm
macropores	d > 50 nm

Sorption curves describe the relation between the sorbed amount and the equilibrium pressure of the gas, recorded at constant temperature. They are also known as sorption isotherms. When both, the adsorption and desorption curve do not coincide, a hysteresis is formed. To facilitate a comparison of sorption data, it is recommended to display the sorption isotherms graphically: on the y-axis the amount of adsorbate Δm and on the x-axis the equilibrium relative pressure ($RH = \frac{p}{p^*}$) are plotted. According to K. S. W. Sing et. al [19] physisorption isotherms can be grouped into six types, schematically illustrated in Fig. 2.5a.

The *Type I* isotherm occurs within microporous solids that have a relatively small external surface. The *Type I* isotherm is reversible. The isotherm has a steep increase in the beginning, but Δm approaches asymptotically a limiting value with $RH \to 1$. The uptake is limited by accessibility of the sorptive to the micropores. On a side note, *Type I* isotherms are sometimes wrongly referred to as Langmuir isotherms, but Langmuir isothermes are found only for flat surfaces without pores.

The reversible *Type II* isotherms occur for non-porous or macroporous solids. The steady increase of Δm indicates unrestricted monolayer-multilayer adsorption. At point B in Fig. 2.5a, monolayer coverage is completed and the following linear middle section is the beginning of multilayer adsorption. The last third of the curve represents the final filling of the pores.

The reversible *Type III* isotherms are uncommon. Their form is convex to the x-axis and does not show a distinct point B. There are only a few systems (e.g. nitrogen on polyethylene), which correspond to this type of isotherm.

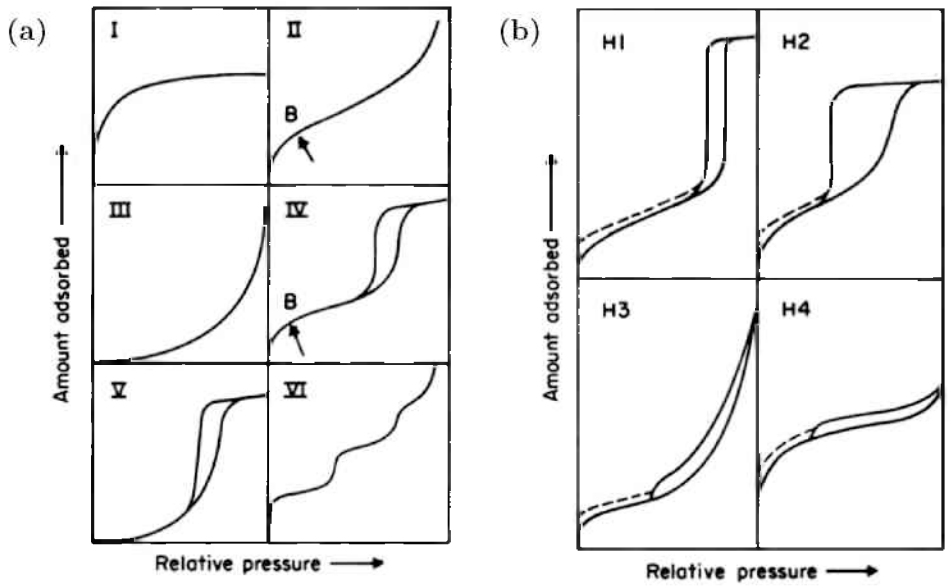

Figure 2.5: Classification of sorption isotherms (a) and types of hysteresis loops (b). The y-axis denotes qualitatively the mass increase Δm and the x-axis denotes the relative pressure ($RH = \frac{p}{p^*}$). After [19].

Type IV isotherms exhibit hysteresis loops. This is associated with condensation in mesopores and a limited water uptake Δm at $RH \to 1$. The adsorption and desorption curves do not coincide. Just as the *Type II* isotherms, point B marks the monolayer-multilayer transition.

Type V isotherms are related to *Type III* isotherms. Their common trait is their weak sorbent-sorbate interaction. The *Type V* isotherm is uncommon, but is found for certain porous sorbents.

The *Type VI* isotherm is obtained at a non-porous surface. The isotherm displays steps. The number of steps depends on the number of multilayers. The sharpness of the steps depends on the sorbent-sorbate system and the temperature. The step height points to the capacity for each adsorbed layer.

Hysteresis loops occurring with multilayer physisorption, are associated with capillary condensation in mesopore structures. In the capillaries, a lowering of vapor pressure takes place. This is caused by adhesion forces at the capillary, respectively pore walls of mesopore structures. The wide range of hysteresis types can be basically characterized by two extreme types, *H1* and *H4*, shown in Fig. 2.5b [19].

In *H1* the adsorption and desorption are almost vertical and nearly parallel. This indicates uniform pores with a narrow size distribution. Whereas in *H4* the two branches remain horizontal and nearly parallel. This is caused by narrow slit-like pores. Other types of hysteresis loops, like *H2* and *H3*, may be regarded as intermediate between *H1* and *H4*. It is not yet understood, which factors contribute towards forming a hysteresis loop, however, the shapes of hysteresis loops have been correlated with spe-

cific structures. *H1* hysteresis loops are associated with porous materials, consisting of agglomerates or compacts of nearly uniform arranged spheres.

Porous adsorbents with not well defined pore size and shape tend to yield *H2* loops. These *H2* loops are difficult to interpret. The difficulty with the interpretation was attributed to the delay of condensation and evaporation processes in bigger pores, which are connected to the surface by smaller pores that are still filled with condensation products. This model is referred to as *ink-bottle* pore [20,21]. It is now recognized as an over-simplified model. Current studies incorporate additionally the effects of finite geometry, network behavior and disordered pore networks [22–24].

Type *H3* loops do not exhibit any limiting adsorption at high relative pressure. Their behavior is associated with aggregates of plate-like particles forming slit-shaped pores, similar to *H4* loops.

The phenomenon of *low pressure hysteresis*, which is associated with micropores, is indicated by the dashed lines in Fig. 2.5b. At the lowest attainable pressures, the removal of the residual adsorbed material can only be achieved at higher temperatures. This may be interconnected with an irreversible chemical interaction of the molecule with the adsorbent, an irreversible uptake of a molecule in a pore (e.g. molecule and pore are of the same size) or swelling of a non-rigid porous structure.

2.3 Atomic force microscopy

In atomic force microscopy (AFM), the surface is scanned by a sharp tip at the end of a cantilever [25]. The movement in x, y, and z directions is realized by employing piezo actuators. In most commercially available systems, a split photodiode detects the laser beam reflected by the back side of the cantilever, as depicted in Fig. 2.6. This way, the split photodiode is able to detect the deflection, as well as the torsion of the cantilever. The topography is recorded as $z(x, y)$.

There are three principle operation modes for AFM: contact mode, non-contact mode [26], and intermittent contact mode [27].

In contact mode, the deflection is held constant with a feedback loop. During the scan, the tip is in permanent contact with the surface. This permanent contact has a risk to influence or even damage the surface of soft materials - as are under consideration here - due to high lateral forces.

In non-contact mode, the cantilever is excited at its resonance frequency f_r. During the scan, the cantilever oscillates without the tip touching the surface. In this non-contact mode, f_r is kept constant by varying z due to interactions between the cantilever and the surface. While in general non-contact mode yields high resolution and has a low likelihood to influence the surface, this can be achieved usually only in ultra-high vacuum.

The intermittent contact mode (also called semi-contact mode, tapping mode or AC mode) is a compromise between the two previous operation modes. Here, the cantilever is excited slightly below f_r. The tip apex is periodically touching the surface of the sample and the oscillation amplitude is kept constant to record the surface

topography [10].

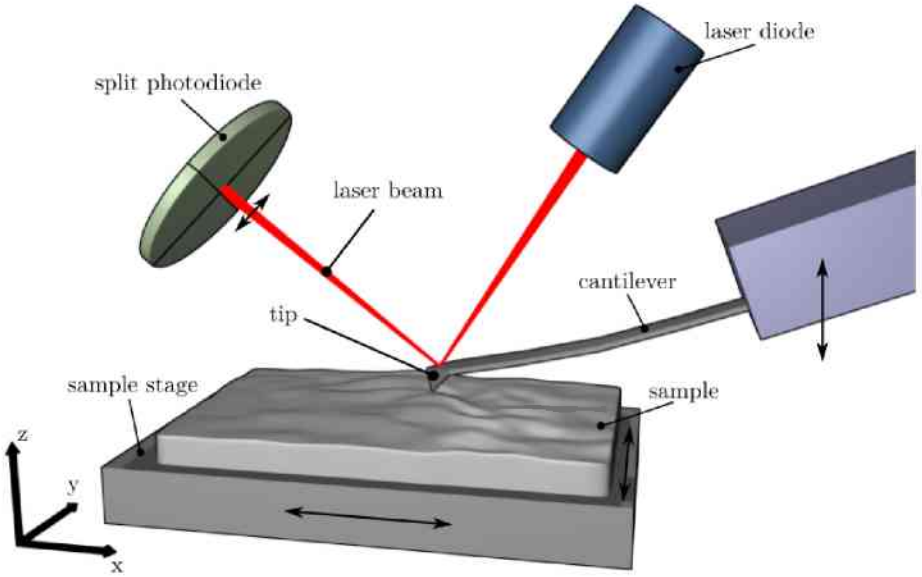

Figure 2.6: An illustration of the principle of AFM measurements [5].

2.3.1 Methods of AFM image analysis

The obtained experimental data from AFM imaging can be analyzed with software supplied by the various AFM manufacturers or with the free software Gwyddion [28]. Gwyddion implements various data evaluation methods for topography analysis such as the height-height correlation function (HHCF) and the fast Fourier transformation (FFT). These methods have already proven their reliability in preceding works on characterization of fiber surfaces [5,10,29–31] and inorganic surfaces [32,33]. The following methods of AFM image analysis are derived from [5,10].

The analysis of the HHCF yields information about the surface roughness. The general appearance of the 2D HHCF $C(r)$ is given in equation 2.3

$$C(r) = \langle [z(r_0 + r) - \langle z \rangle] [z(r_0) - \langle z \rangle] \rangle \,. \tag{2.3}$$

Here, the vector r is a point on the surface ($\mathrm{x_i}$,$\mathrm{y_j}$) and z holds the height information $z(x_\mathrm{i}, y_\mathrm{j})$. However, we have to deal with a finite sample size, hence the AFM images are finite M × N matrices. The 2D HHCF can be rewritten for use on a discrete height map

$$C(m,n) = \frac{1}{(N-n)(M-m)} \sum_{k=1}^{N-n} \sum_{l=1}^{M-m} z_{k+m,l+n} z_{k,l}. \tag{2.4}$$

In the height map $m = \frac{x_1 - x_2}{\Delta x}$ and $n = \frac{y_1 - y_2}{\Delta y}$, where (x_i, y_j) are data points with Δx and Δy as intervals in their respective directions. In Gwyddion, all horizontal scan lines are averaged and implemented as single scan line, thus, resulting in an one-dimensional (1D) HHCF, displayed in equation 2.5.

$$C_x(m) = C(m, 0) = \frac{1}{N(M-m)} \sum_{k=1}^{N-n} \sum_{l=1}^{M-m} z_{k+m,l} z_{k,l} \tag{2.5}$$

However, to extract topographical information from the calculated 1D HHCF, fitting with a model is necessary. A fitting function for a self-affine random rough surface with a cut-off in roughness increase,

$$C(x) = \sigma^2 e^{-\left(\frac{|x|}{\xi}\right)^{2\alpha}}, \tag{2.6}$$

is applied. For further details see [33] and references therein. Equation 2.6 is characterized by the parameters σ, ξ and α. Fig. 2.7 displays an exemplary fit.

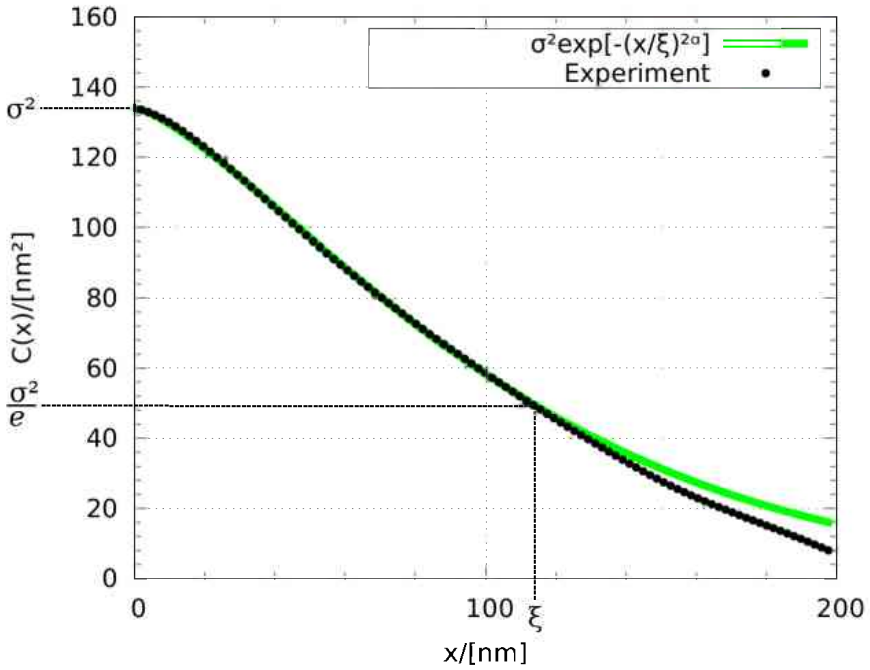

Figure 2.7: Exemplary fit for a self-affine random rough surface with a cut-off based on equation 2.6. The black dots represent the calculated 1D HHCF from experimental data. The fit is represented by the green line. The roughness parameters σ, ξ, and α can be extracted from the fit.

The root mean square (RMS) roughness of the surface is denoted as σ and is calculated by

$$\sigma = \sqrt{\frac{1}{N^2} \sum_{i=1}^{N} \sum_{j=1}^{N} [z(x_i, y_j) - \langle z \rangle]^2}. \tag{2.7}$$

The lateral correlation length ξ is a measure for the maximum distance between two points, that are still considered correlated. The physical meaning of ξ is illustrated in Fig. 2.8, where two surface profiles with different values for ξ, but with constant values for both σ and α, are depicted [5,10,34]. In comparison, the profile in Fig. 2.8b has more alterations on the same lateral distance than the profile in Fig. 2.8a.

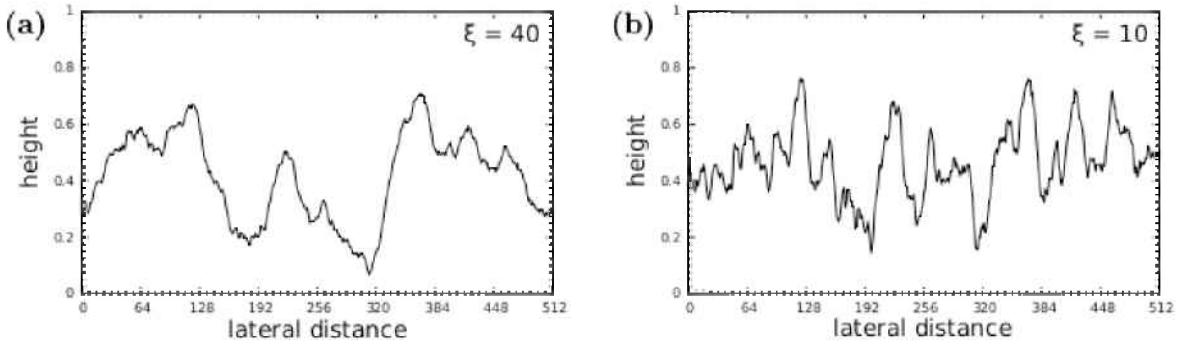

Figure 2.8: Simulated surface profiles for different lateral correlation lengths ξ. Both profiles have the same values for σ and α, but in (a), ξ is four times larger than in (b). From [10].

α is called Hurst parameter and can be considered as the jaggedness of the surface. Comparing the influence of α on the profiles in Fig. 2.9, the reason for the term jaggedness is obvious. A surface with a low Hurst parameter, as seen in Fig. 2.9b, would be considered more rugged than a surface with a high α (Fig. 2.9a). It should be noted that equation 2.6 becomes invalid for $\alpha \rightarrow 0$.

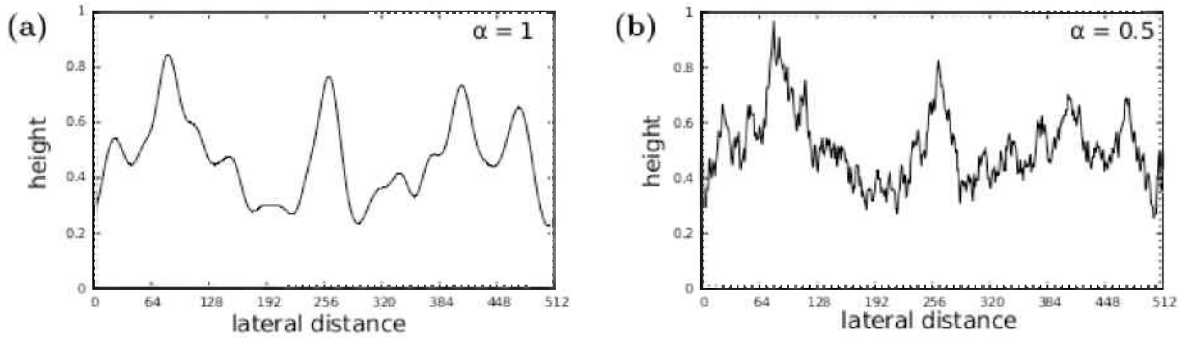

Figure 2.9: Simulated surface profiles for different Hurst parameters α. Both profiles have the same values for σ and ξ, but in (a), $\alpha = 1.0$ and in (b), $\alpha = 0.5$. From [10].

FFT analysis gives information about preferred feature arrangements and harmonic components of an image. It is restricted by the number of transformable data points in the form of 2^n. All images presented here have been recorded in a 512×512 pixel or 1024×1024 pixel matrix. The FFT [35] algorithm utilizes the FFTW3 library. In contrast to the classical FFT algorithm, new implementations like the FFTW3

library are not bound by the 2^n restriction [36]. The FFT diagrams presented here are FFT(z(x,y)) - the Fourier transform of the topography images.

3 Experimental

3.1 Sample preparation

3.1.1 Sorption balance

In order to differentiate between fiber network and single fiber sorption behavior, two ways of sample preparation were devised. A sample bowl (Fig. 3.1a) to determine single fiber properties and a wire cage setup, as is shown in Fig. 3.1b, to test for network properties.

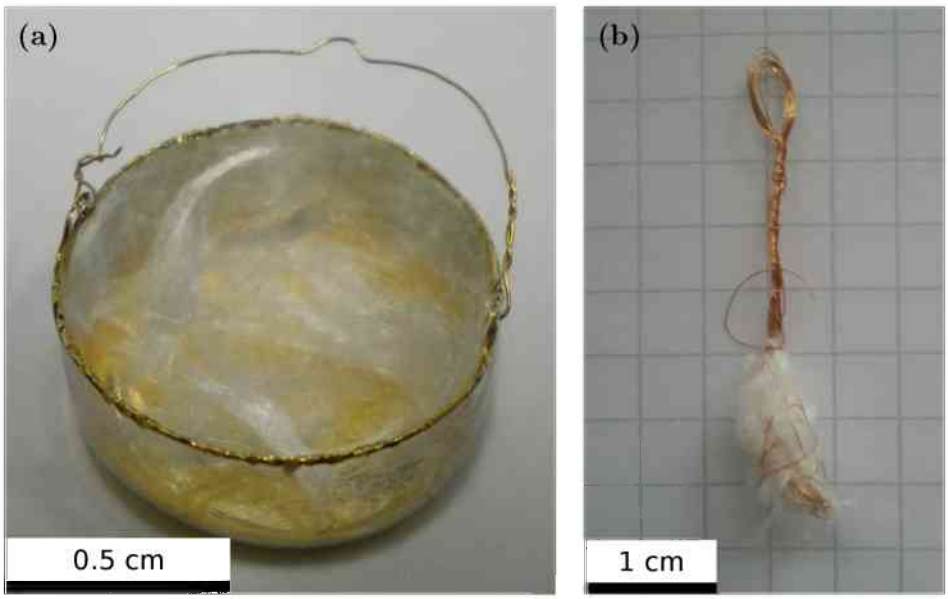

Figure 3.1: Image of the loose bundle in the sample bowl (a) and the close packed viscose fibers in the wire cage (b).

The sample bowl is made of quartz glass covered by a hydrophobic gold coating and is 10 mm in diameter and 6 mm in height. The gold coating ensures that water will adsorb mainly on the sample under investigation and not the sample bowl. At first, adsorption measurements with single fibers (about 50 isolated fibers) were tried. The balance possesses the necessary accuracy for such measurements and consists of two symmetrically arranged bowls that should correct the water absorption of the bowls. However, as it turns out the water adsorption on the sample bowl is not negligible when the sample mass is much lower than 20 mg. The difference is very likely related to scratches, caused from changing the samples. Thus, the minimal mass of fibers

was set to a loose bundle of roughly 20 mg which corresponds to about 20,000 fibers with 2 dtex and 5 mm length. In this case, the influence of the sample bowl's water adsorption is about 1 %, compared to the sample mass. With this knowledge, the obtained relative water uptake needs to be corrected by the water uptake of the sample bowl. With respect to the average amount of adsorbate, a value of about 0 % to 3 % in relative water uptake has to be subtracted from the obtained results.

The network behavior was measured by a wire cage setup. Here, too, fibers with a dry mass of about 20 mg were prepared, but this time tightly packed by a copper wire. Initially, the wire is formed into a wire whisk. After placing the previously compressed fibers in the whisk, the wire is tightened by rotating the fibers together with the wire to form the mounting that is depicted in Fig. 3.1b. The provided pulp fibers were already in a dense packed state. In their case, instead of employing the wire cage to pack them tightly together, a chunk of pulp fibers was directly put on the hook of the microbalance to measure their network behavior. The fiber types investigated with the sorption balance are detailed in table 3.1. The viscose fibers (Fig. 3.2) were taken from the production cycle, the pulp fibers, a mixture of spruce and pine, were taken after first refinement of the raw material.

Table 3.1: Overview of the samples for the sorption balance.

name	type	cross-section	dtex	length
Verdi	viscose fibers	cloud-shaped	1.7	6 mm
Bellini	viscose fibers	hollow and collapsed	2.1	4 mm
Danufil	viscose fibers	cloud-shaped	1.7	5 mm
Pulp fibers	pulp fibers			

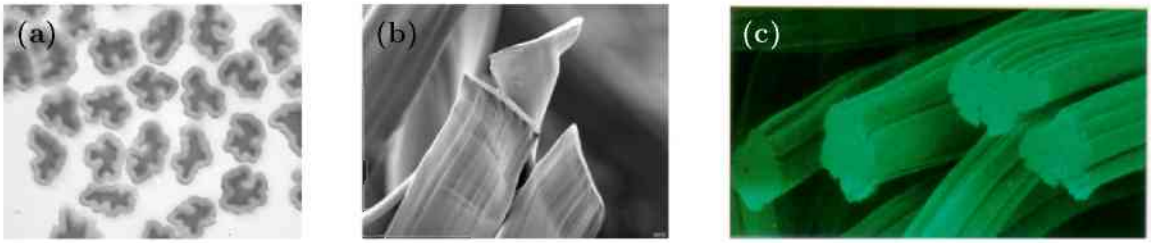

Figure 3.2: SEM images of the viscose fibers measured with sorption balance. (a) Verdi (b) Bellini (c) Danufil. From [37] with permission.

3.1.2 AFM imaging

To reliably record AFM images on a single fiber, the fiber was fixed on a randomly scratched silicon substrate. The random scratches were made to aid in the relocation of a formerly investigated region. The substrate was fixed on a commercial steel sample holder with double-sided adhesive tape. To avoid cringing and buckling, the fibers were

strained and fixated with adhesive tape on both ends, as schematically displayed in Fig. 3.3.

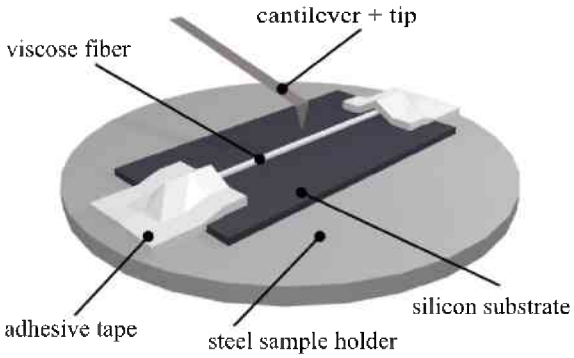

Figure 3.3: Sketch of the finished sample preparation for AFM imaging.

Two sets of fibers were provided by the manufacturer and are listed in table 3.2. Each set consists of samples from two different batches, which differed in their capacity to take up water. However, all batches were produced under similar conditions. All fibers are viscose type fibers and are called Galaxy by Kelheim Fibres. The samples were taken immediately from the production cycle.

For the morphological analysis of the recorded AFM images, the free software Gwyddion was used [28]. All AFM images were preprocessed with Gwyddion using step line correction and levelling the data points by subtracting a mean plane. Step line correction aims to align adjacent scanlines to each other, so that sudden artificial jumps are corrected. The resulting images are presented as false color images, where the bright areas in the AFM height images represent elevated areas, whereas the dark areas are lower areas.

Table 3.2: Properties and measurement conditions of viscose fibers investigated by AFM. The average diameter d of the investigated fibers was determined from optical micrographs (OM). The samples were measured under ambient conditions, with temperature T and relative humidity RH given in the table.

set 1	water absorption	type	cross-section	d μm	T °C	RH %
GUG-VY6	high	viscose fibers	trilobal	23 ± 2	22 - 25	15 - 45
GUG-VY8	low	viscose fibers	trilobal	27 ± 6	20 - 22	25 - 59
set 2	water absorption	type	cross-section	d μm	T °C	RH %
VY-384002	low	viscose fibers	trilobal	27 ± 3	18 - 22	31 - 53
VY-384749	high	viscose fibers	trilobal	27 ± 4	21 - 23	20 - 47

During initial measurements, the trenches covering the surface were analyzed man-

ually at first. But due to the large number of trenches and in order to eliminate the subjectivity in deciding whether a surface feature is considered as a trench or not, an automated trench count procedure was created. In a preliminary attempt, Gwyddion's watershed method was utilized. In this method, a water droplet follows the steepest descent path to minimize its potential energy. In general, there are three parameters: drop size, threshold, and number of steps. However, facing the curvature and the bumpy surface, watershed yielded too unreliable results. Additionally, parameter tuning depended highly on the operator and still took a fair amount of time (about 10 min per image).

Afterwards, a script using the MATLAB environment [38] was developed. The task of the script is to determine the trench density for further statistics. The source code is listed in Appendix A. A comparison between manual and automated trench count is presented in Fig. 3.4a and 3.4b, respectively. The automated script still needs the manual input of thresholds for each image. However, with an average calculation time of 20 seconds per image, the MATLAB script outperforms the manual counting (which takes about 20 min per image) significantly. Additionally, the MATLAB script is presumably far more unbiased than a human operator. At this point it should be clarified that both, the manual and the automated method, use different principles to count trenches and thus, are not comparable to each other. The manual count represents a linear fit for every detected trench on the surface. Due to that, a directional change of the trench of an angle of about 20° was counted as a new trench. On the other hand, the MATLAB script employs an edge detection procedure. Among the common edge detection algorithms like Sobel, Canny, Prewitt, Roberts, and fuzzy logic methods [38], Canny yielded the best results. In principle, the automated script uses two thresholds, one approaching the surface from below, the other approaching the surface from above. This way, the trenches and surface impurities can be detected separately and overlaps can be avoided. To avoid the count of the vertical ripple structure, the edge detection was used on the derivative of the surface in y-direction. This favors the detection of horizontally aligned trenches, as shown in Fig. 3.4b.

3.2 Sorption balance setup

The sorption balance employed here is a home-built and semiautomatic device that measures gravimetric gas or vapor uptake and release in order to record sorption isotherms [39,40]. This way, the mass of an absorbed gas or vapor is measured directly [19]. In this work, only vapor from distilled water was used. The measurement of the mass is realized by a symmetric two-pan vacuum ultra-microbalance (Sartorius Instruments, model S3D), capable of an accuracy of up to 0.1 μg [41]. In order to measure the vapor pressure, two pressure gauges were employed. The temperatures of the sample, the reservoir and the laboratory are controlled and kept constant. The room temperature is controlled by air-conditioning. In order to record a sorption isotherm, the sample is exposed to the vapor at predefined pressures. After an equilibration time of 10 minutes, the mass uptake is recorded and the process is repeated for other pres-

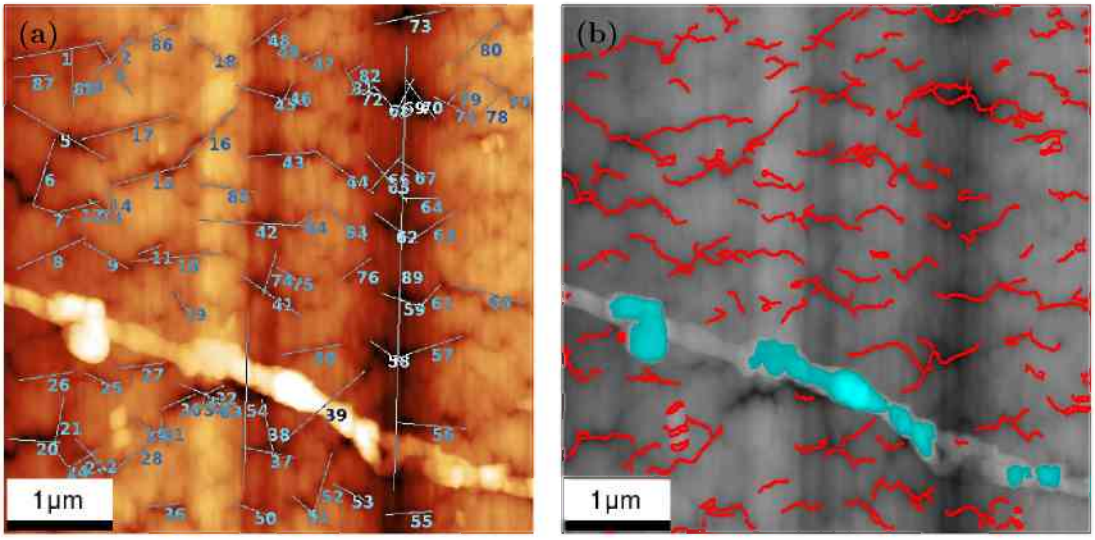

Figure 3.4: Comparison of the manual trench counting (a) to the MATLAB script (b). The blue marked areas are impurities.

sures until the saturation pressure is reached. Subsequently, the desorption isotherm is recorded by equilibrating the sample while lowering the pressure. The procedure is managed by a computer program.

The scheme and the actual image of the sorption balance are displayed in Fig. 3.5a and Fig. 3.5b, respectively. The sorption balance basically consists of an sorption branch, which provides the vapor and a desorption branch to establish a vacuum. The desorption branch is equipped with a rotary vane vacuum pump (Pfeiffer), a computer controlled electromagnetic valve and a dosing valve. The sorption branch, which actually denotes the processes of adsorption and absorption, is built symmetrically to the desorption branch, but with a temperature controlled reservoir instead of the vacuum pump. The reservoir has a lock valve to evacuate it separately. Its temperature is regulated by a water bath and is set between 23 °C – 25 °C. The corner valve - when opened enables the evacuation of the whole device via the rotary vane pump. The parts are connected by flexible steel tubes that are wrapped by a heating band in order to bake out residuals at 200 °C. The microbalance is covered by two glass cylinders – one for the sample and one for the reference mass – which are covered by graphite to make the inner cylinder surface hydrophobic. The glass cylinders with the sample and the reference mass are put into a water bath at 17 °C. If necessary, the glass cylinders can be baked out by a heating cuff, with a temperature of up to 100 °C. In this study, the samples were not baked out to avoid structural and chemical changes in the cellulosic fibers. Furthermore, the setup is designed to be hydrophobic and with the lowest temperature in the vicinity of the sample to initiate condensation there first.

A short description of the measurement procedure is presented in the following.

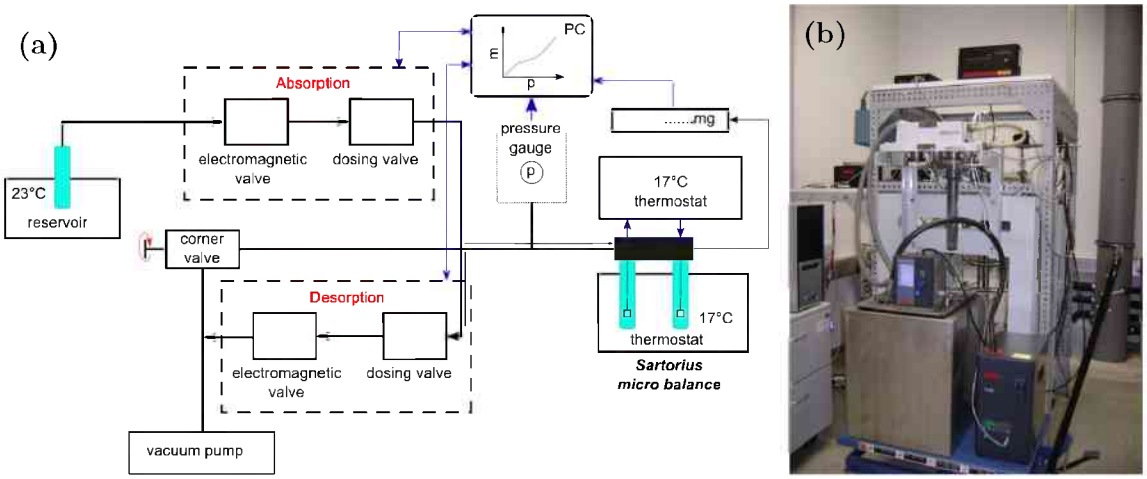

Figure 3.5: (a) Scheme (taken from [40]) and (b) photograph of the sorption balance used in this work.

Measurement procedure

Before measurement

- First measure the sample mass.
- Attach the sample to the microbalance (right side) and equate the counter part (left side), preferentially with gold, due to its hydrophobic nature.
- Fix the glass cylinders on both sides.
- Start evacuation of the whole device.
- Evacuate at least for 12 hours with the option to bake out the sample with heating cuffs up to a temperature of 100 °C (not recommended for cellulosic fibers).
- Lower the glass cylinders into the water bath and wait for another 10 hours to equilibrate the system.

Start measurement

- Close all valves (corner valve and desorption valve).
- Open the lock valve and evacuate the reservoir until the water in the reservoir starts boiling. Then close the lock valve.
- Tare the microbalance to zero and start the computer program after all the desired parameters are inserted.

Remove sample

- After recording the isotherm, open the desorption valve and turn off the vacuum pump.

- Open the inflation valve until atmosphere pressure is reached.
- Remove the water cooling system and glass cylinders.
- Measure the dry mass of the sample with another microbalance.

3.3 AFM Setup

The Atomic Force Microscope model used for this work was an Asylum Research MFP-3D (Santa Barbara, CA) as presented in Fig. 3.6. It is equipped with a planar closed-loop sample scanner. The x, y and z scanners are decoupled and their maximum ranges are 90 μm and 15 μm, respectively. All AFM images were taken in intermittent contact mode. Due to the curvature and rotation of the trilobal fibers the scan size was limited to 5 μm $\times$ 5 μm images. The fibers were arranged perpendicular to the cantilever's long axis in order to verify any correlations between fiber orientation and fiber morphology. Additionally, for every measurement optical images were taken to determine the angle of the fiber axis and the scan position as seen in Fig. 3.7.

Figure 3.6: Photograph of the Asylum Research MFP-3D (Santa Barbara, CA).

3.3.1 AFM Probes

For AFM imaging, exclusively Olympus AC240TS probes were used. These probes are composed of a silicon cantilever, a tetrahedral silicon tip at the very end and a aluminum reflective coating on the back side of the cantilever. Their geometry is indicated in Fig. 3.8 with a front angle of 0°, a back angle of 35° and a side angle of 15°. The tips have a typical apex radius of 9 nm $\pm$ 2 nm and the cantilevers have a spring constant of about 2 N/m. The cantilevers have a rectangular shape with a

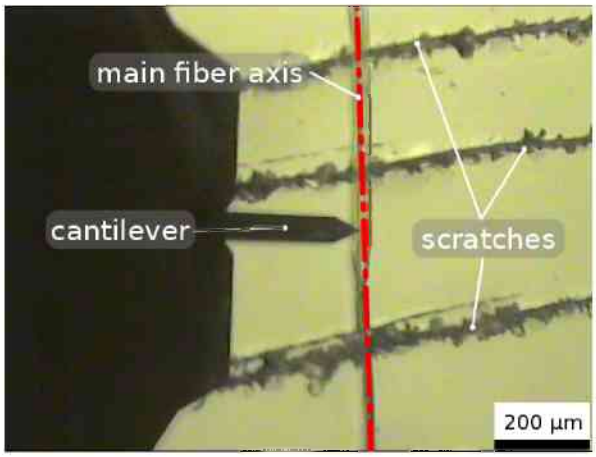

Figure 3.7: OM of a Galaxy viscose fiber, mounted under the AFM.

length of 240 μm, a width of 40 μm and a thickness of 3.3 μm. Their average resonance frequency is 70 kHz.

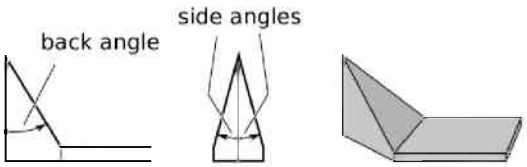

Figure 3.8: A sketch of the Olympus AC240TS probes taken from [10].

4 Results

4.1 Sorption balance results

For the recording of sorption isotherms, several types of viscose fibers as well as pulp fibers were prepared. The objective was to determine differences in the viscose fibers' ability to absorb water and to eventually reference the results to pulp fibers. Based on the limited number of data points in the isotherms, the error in the water uptake was estimated to be about 5 % at most.

4.1.1 Sample bowl

4.1.1.1 First results

For the first sorption measurements, the provided samples did not undergo any preparation prior to inspection. The viscose fibers were delivered as flat 5 $mm \times 5$ mm chips, and the pulp fibers were delivered in a single wet chunk of pulp. In the initial recordings of sorption isotherms, the sample bowls were simply filled to brim with the provided samples.

In all the sorption isotherms presented in the following, the adsorption data is connected by solid lines, whereas a dashed line is used for the presentation of the desorption curves. Fig. 4.1 represents the recorded sorption isotherm of Bellini type viscose fibers. Due to the limitations of the construction, the isotherms start around a relative vapor pressure of 0.02 ± 0.02. (The term relative vapor pressure is equivalent to the relative humidity and can be abbreviated either with $\frac{p}{p^*}$ or RH.) The transition from monolayer to multilayer adsorption, although not very accentuated, is located at RH ≈ 0.1. According to Fig. 2.5a, this transition point is indicated by an arrow in Fig. 4.1. The shape of the hysteresis loop is an intermediate between *H2* and *H4* (see Fig. 2.5b). The adsorption curve at high RH does not seem to exhibit any limiting adsorption. This might be correlated to the interconnectivity of the pores and/or to the interaction potential between sorbent and sorptive [19,40]. One has to state that this makes the characterization of the isotherm, and therefore of the fibers, difficult. The shape of the sorption isotherm indicates the presence of macro-, meso-, and micropores [19,40]. The determination of the relative water uptake was performed manually. In this work, the relative water uptake was defined as the transition point to the drastically increasing water uptake. This point was chosen, because after this point the events occurring on the sample are unclear and water might be already condensing in the sample bowl, which would yield no information about the sample. The determination of the water uptake can be aided by the equilibration time of each point of the curve. Starting at the

transition point, the time for equilibration increases due to the increasing amount of water uptake. In this manner, the relative water uptake was determined at $RH \approx 0.9$ with 23 %. The horizontal section at the beginning of the desorption curve can be caused by the interconnectivity of the pores, holding back the water, and/or effects caused by the fiber network [19,39,40].

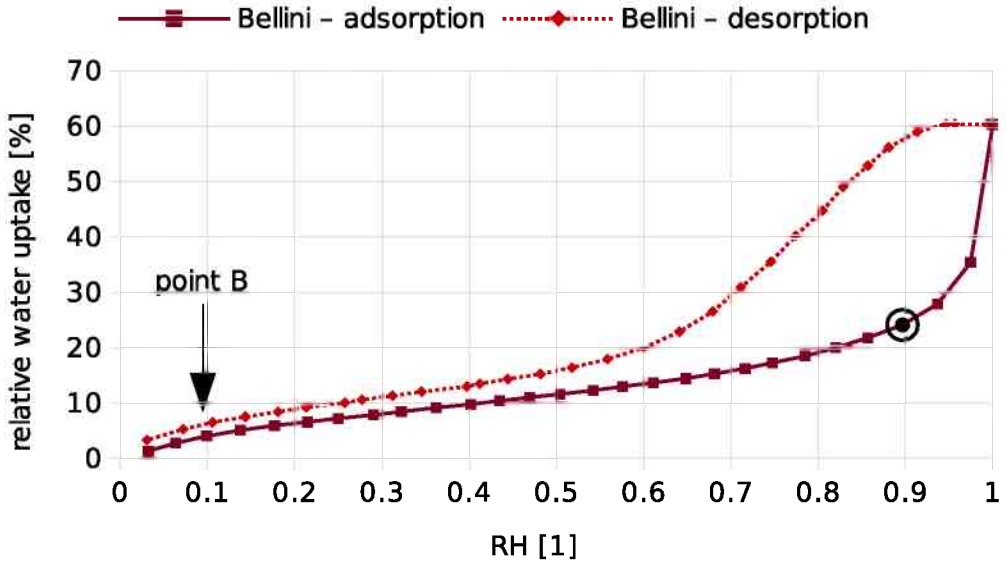

Figure 4.1: Sorption isotherm of Bellini fibers at 17 °C. The solid line denotes the adsorption curve and the dashed line denotes the desorption curve. The mass of the dried fibers was 57.1 mg. The black circles denote the point, which was used to determine the water uptake.

Fig. 4.2 represents the recorded sorption isotherm of Verdi type viscose fibers. The isotherm resembles the *H4* hysteresis loop, illustrated in Fig. 2.5b. Compared to Fig. 4.1, the drastic increase in water uptake is not very accentuated. This was likely caused by problems with the air-conditioning in the room. Occasionally, the temperature in the room - with the sorption balance installed - increased, thus increasing the saturation vapor pressure of water up to 25 mbar. Since this is a parameter that has to be inserted manually beforehand in the software, the saturation pressure was not reached. In this case, $RH = 1$ actually represents the highest achieved pressure of 19.48 mbar. The saturation pressure of water vapor at 17 °C is 19.33 mbar. This problem was fixed in measurements of the 20 mg series and the wire cage. Other possible obstructions, capable of shifting or apparently shifting the thermodynamic equilibrium, are condensation in the cables of the sorption balance, condensation near the pressure gauge or a temperature change in the laboratory. For the former two cases, the only available solution is baking out the whole construction. Still, aided by the equilibration time the relative water uptake was determined with 21 %. The shape of the hysteresis loop suggests the presence of micro-, meso-, and macropores [19,40]. The monolayer to multilayer transition is roughly located at $RH \approx 0.2$.

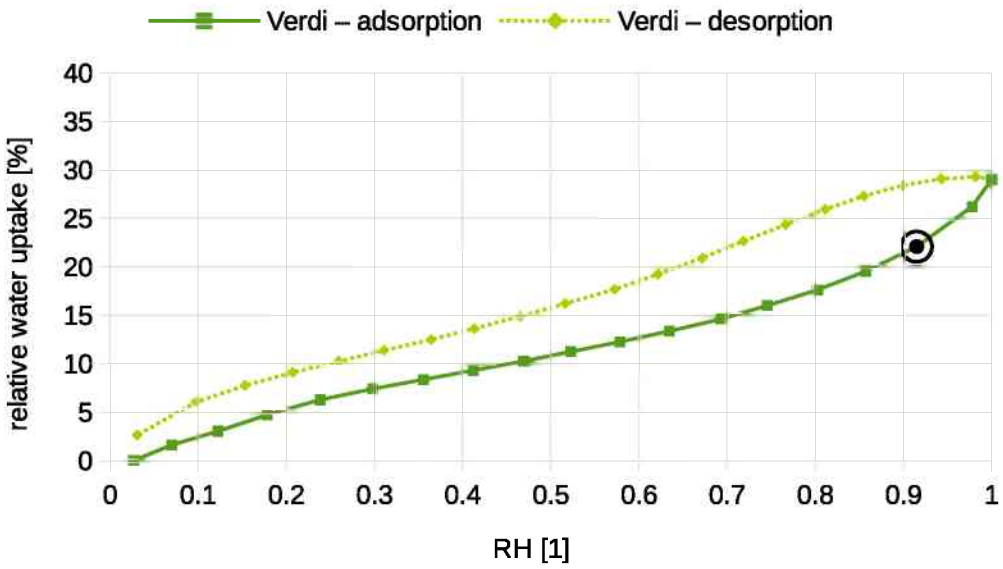

Figure 4.2: Sorption isotherm of Verdi fibers at 17 °C. The mass of the dried fibers was 94.6 mg.

Fig. 4.3 represents the recorded sorption isotherm of Danufil type viscose fibers. The recording of the isotherm faced similar problems like the recording of the isotherm presented in Fig. 4.2. Additionally, the desorption loop was lost, due to computer problems. The transition point between monolayer and multilayer adsorption is clearly visible at $RH \approx 0.1$. The relative water uptake was 18 %. The missing desorption curve makes the further interpretation of the hysteresis loop impossible.

The shape of the sorption isotherm of pulp in Fig. 4.4 is similar to the shape in Fig. 4.1. The indications of the three pore types, micro-, meso-, and macropores, are present. The micropores are indicated at low RH of the hysteresis. If there were no micropores present, the hysteresis loop would be closed at low RH. Macropores are found at high RH [19,39,40]. The interval $0.6 < RH < 0.9$ of the desorption curve marks the evaporation on the surface and in easy accessible pores. Still, at high RH the interference of different pore sizes, multilayer adsorption and network effects make a quantitative analysis impossible. An odd effect can be seen at high RH on the desorption curve. While RH is decreasing, the relative water uptake actually increases slightly for a short time. This was likely caused by a change of the thermodynamic equilibrium, namely, an increase of the room temperature during the recording of the desorption curve or condensation somewhere within the sorption balance. However, this did not impact the adsorption curve, which yielded a relative water uptake of 17 %.

4.1.1.2 20 mg series

In the following chapter, the attempted characterization of isolated single fibers is described. For these measurements, 50 isolated fibers of each viscose fiber type were

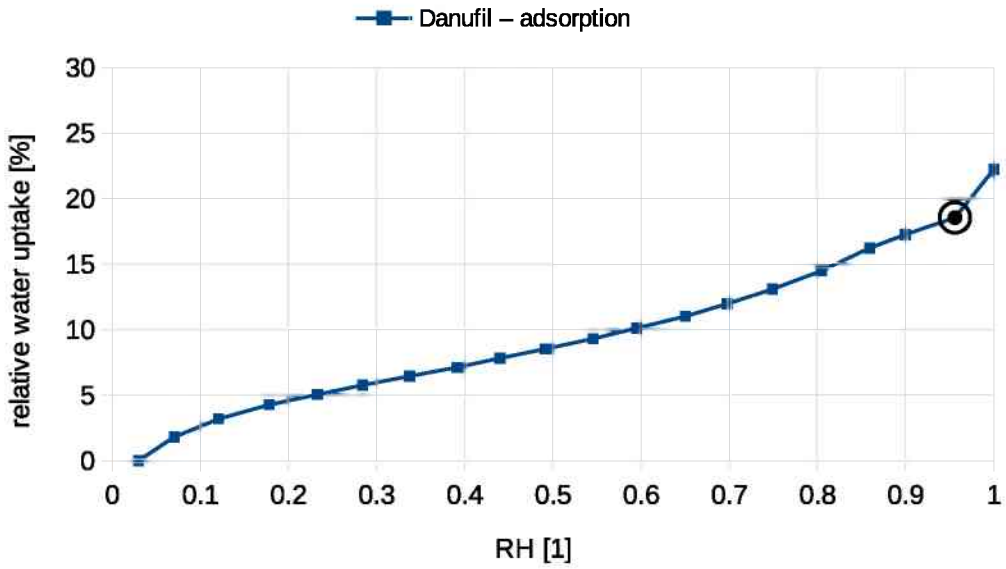

Figure 4.3: Adsorption isotherm of Danufil fibers at 17 °C. The mass of the dried fibers was 129.8 mg.

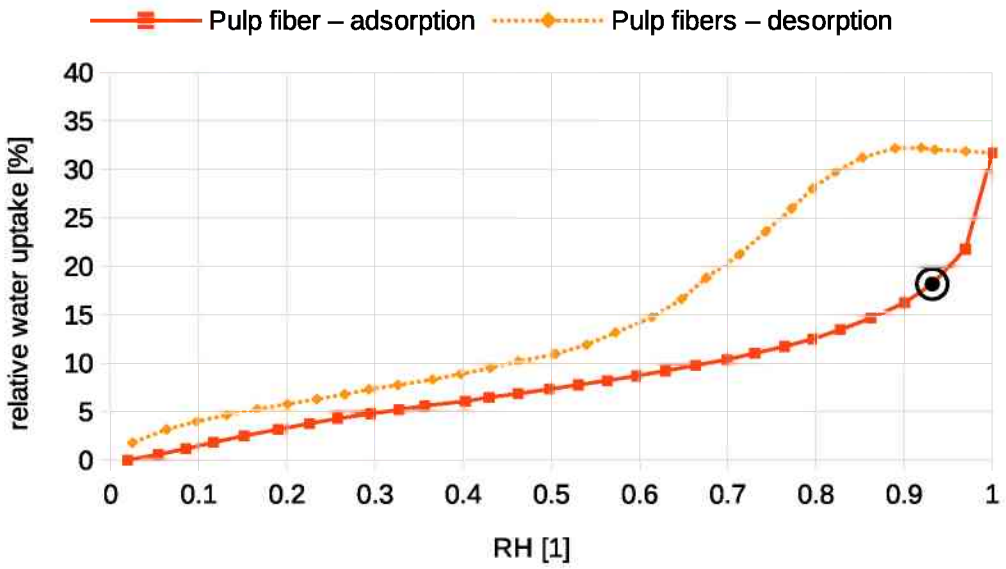

Figure 4.4: Sorption isotherm of pulp fibers at 17 °C. The mass of the dried fibers was 81.8 mg.

prepared. All sorption isotherms recorded were almost identical.

The adsorption isotherm of the empty sample bowl is presented in Fig. 4.5 and revealed that it is identical to the bowl filled with 50 single fibers (about 50 μg). Hence, the single fiber measurements were stopped. Nominally, the adsorption and desorption

of the sample bowl and its counter part on the two-armed microbalance should cancel each other out. Due to the frequent change of samples with tweezers, the gold coating on the sample bowl was damaged. Numerous scratches were observed. Those scratches exhibit micro- and mesopore behavior.

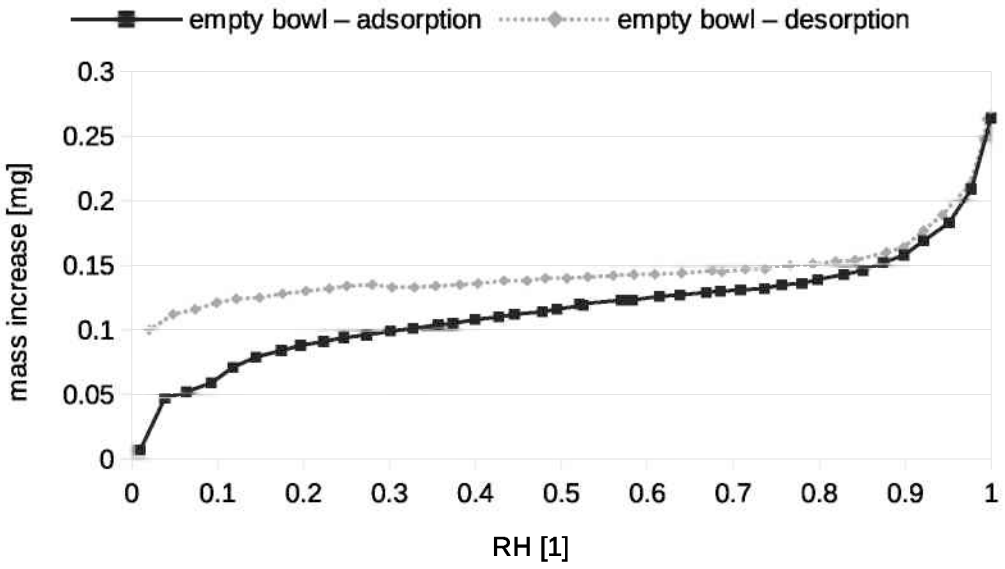

Figure 4.5: Sorption isotherm of the empty sample bowl at 17 °C.

In accordance with the results obtained from the empty sample bowl in Fig. 4.5, the minimum amount of the sample mass was set to roughly 20 mg, so that the influence of the sample bowl's adsorption would be less than 1 %. Usually, the viscose fibers already contain humidity, when they are prepared for the measurement. In order to compensate for that an initial sample mass of roughly 30 mg was selected. For the following evaluation of the results of the 20 mg series, the adsorption of the sample bowl was taken into account and accordingly adjusted. For this, the amount of water adsorbed by the sample bowl - extracted from Fig. 4.5 - was subtracted from the total amount of adsorbed water. Note that for the 20 mg series, the fiber samples were arranged in loose bundles to mainly measure single fiber properties.

Fig. 4.6a represents the recorded sorption isotherm of Bellini type viscose fibers. The sorption isotherm resembles the *H4* hysteresis loop, which is associated with slit-shaped pores and plate-like particles. In case of viscose fibers, this can be attributed to surface ripples, parallel to the main fiber axis. The loose fiber bundles should not experience much network interactions, which should therefore not interfere with the measured adsorption at high RH. This hints at the isotherm being close to single fiber behavior. The very short horizontal section at high RH of the desorption curve is followed by the evaporation from easy accessible pores. The mesopores are the main reason for forming a hysteresis loop in the first place [19,39,40]. An indication that micropores are present is that sorption and desorption curves do not coincide at low RH. In order to determine the relative uptake, in addition to comparing the equilibration time, the

derivative of the adsorption curve was calculated, which is presented in Fig. 4.6b. Due to higher sensitivity, the derivative of the adsorption curve makes the point of transition to an increasing water uptake easier to detect. The point, which was used to determine the water uptake is marked by black circles in both, the sorption isotherm and the derivative of the adsorption curve. The relative water uptake was 20 %.

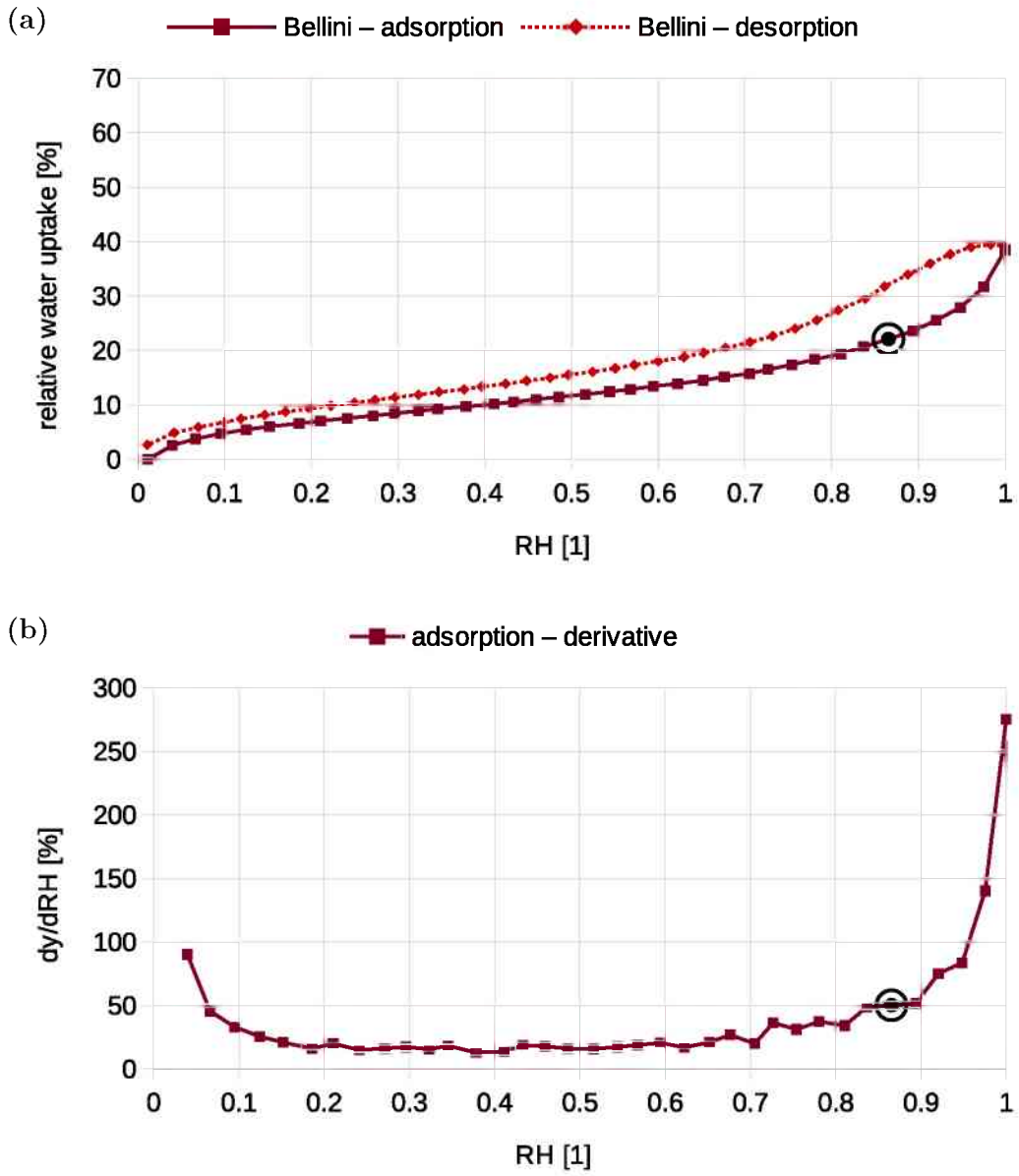

Figure 4.6: (a) Bellini fiber sorption isotherm of the 20 mg series fibers at 17 °C. The mass of the dried fibers was 26.2 mg. (b) Derivative of the adsorption curve.

The shape of the sorption isotherm for Verdi type viscose fibers is presented in Fig. 4.7a. It resembles the shape of the sorption isotherm for Bellini type fibers,

presented in Fig. 4.6a. The isotherm correlates to the *H4* loop. Again, this might hint towards single fiber behavior. Fig. 4.7b represents the derivative of the sorption isotherm. At $RH = 0.8$ a small anomaly, marked by an arrow, can be detected. With its sensitivity, the derivative curve can also be used to investigate anomalies during equilibration. The anomaly occured close to the transition point, within a time frame of roughly 50 minutes. It is possible that the equilibration time was too short for a measurement this close to the transition point. However, the effect is hardly visible on the adsorption curve. The relative water uptake of this sample was 20 %.

Fig. 4.8a represents the recorded sorption isotherm of Danufil type viscose fibers. The shape of the hysteresis loop is an intermediate between *H2* and *H4* loops. The overall shape has close resemblance to *H4* with both curves being almost parallel to each other and close to the horizontal axis, except for high RH. The desorption curve looks closer to *H2*, but without the vertical decrease characteristic for *H2* loops. The hysteresis looks very similar to the hysteresis of Fig. 4.1. Both share basically the same properties. Again, a small anomaly, marked by an arrow, can be detected, that is more pronounced in the derivative of the adsorption curve, as presented in Fig. 4.8b. The manual analysis of the sorption isotherm yielded a relative water uptake of 20 %.

Fig. 4.9 represents the recorded sorption isotherm of pulp fibers for comparison. The shape of the hysteresis is close to *H2* and actually reminds one of a bird's silhouette. At high RH, the darker adsorption and the brighter desorption curve are horizontal. This might indicate that all accessible pores are filled with water and condensed water is present on the outer surface. In other words, the outer and inner surfaces are saturated. Within the interval $0.5 < RH < 0.6$, a sudden and almost vertical decrease can be seen in the desorption curve. The sharpness of this feature corresponds likely to easy accessible macropores and condensed water on the outer surface. From there, the transport to the other pores takes place. Only at low RH values, micropores which do not release the adsorbed water due to strong interaction forces determine the desorption behavior [19,39,40]. The manual analysis of the adsorption curve resulted in a relative water uptake of 18 %. It should be noted, that the sample mass of the dried pulp fibers was 91.2 mg. The pulp fibers were in a wet state from the beginning, containing a large quantity of water. The amount of water was simply overestimated, during the preparation of the pulp sample.

4.1.2 Wire cage

Using a wire cage is a different way of sample preparation that has been employed here. Instead of a loose bundle of fibers, the fibers are tightly packed into a wire cage. With this setup, a significant influence of the fiber network was expected due to capillary condensation. For this, the number of recorded data points was increased. Since the sample bowl is not used for this sample configuration, the previous restriction to the sample mass did not apply here. During preparation of the wire cage, a lot of fibers were lost, thus the sample masses differ greatly from each other.

Fig. 4.10 represents the recorded sorption isotherm of Bellini type fibers in the wire cage series. Compared to the Bellini sample in the 20 mg series (Fig. 4.6a), their shapes

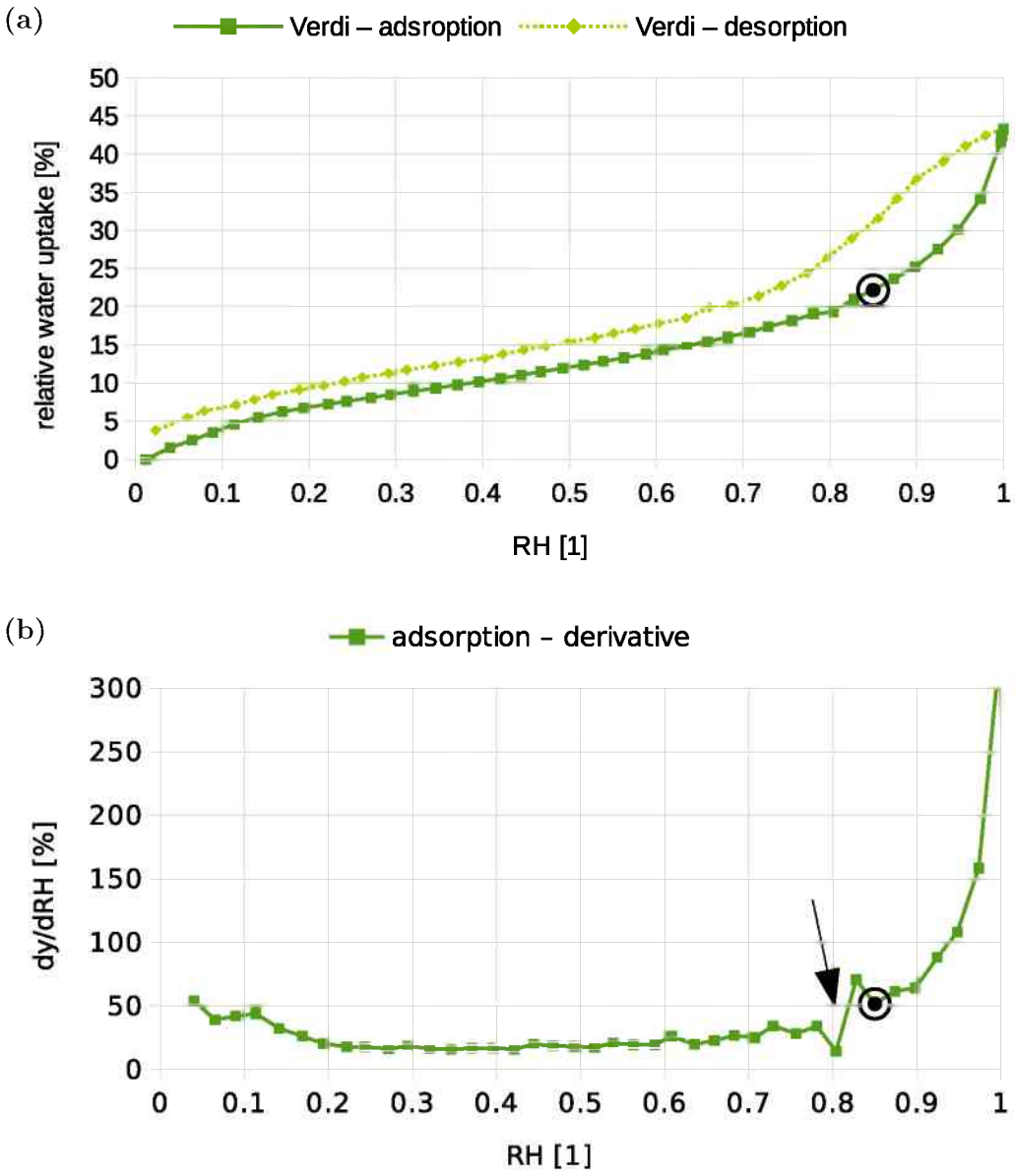

Figure 4.7: (a) Verdi fiber sorption isotherm of the 20 mg series fibers at 17 °C. The mass of the dried fibers was 24.2 mg. (b) Derivative of the adsorption curve. An anomaly in the curve is indicated by an arrow.

differ notably. While the hysteresis in the 20 mg series is closer to a *H4* loop, the wire cage hysteresis resembles more that of the *H2* loop. Similar to the previous pulp fiber sample in the 20 mg series, saturation occurs at high RH. Between 0.7 RH and 0.8 RH, a decrease in water uptake is detected in the desorption curve. This decrease corresponds to easy accessible macropores and the outer surface of the fibers, similar to the pulp fiber sample. However, the decrease is not as sharp and distinguishable in comparison. If

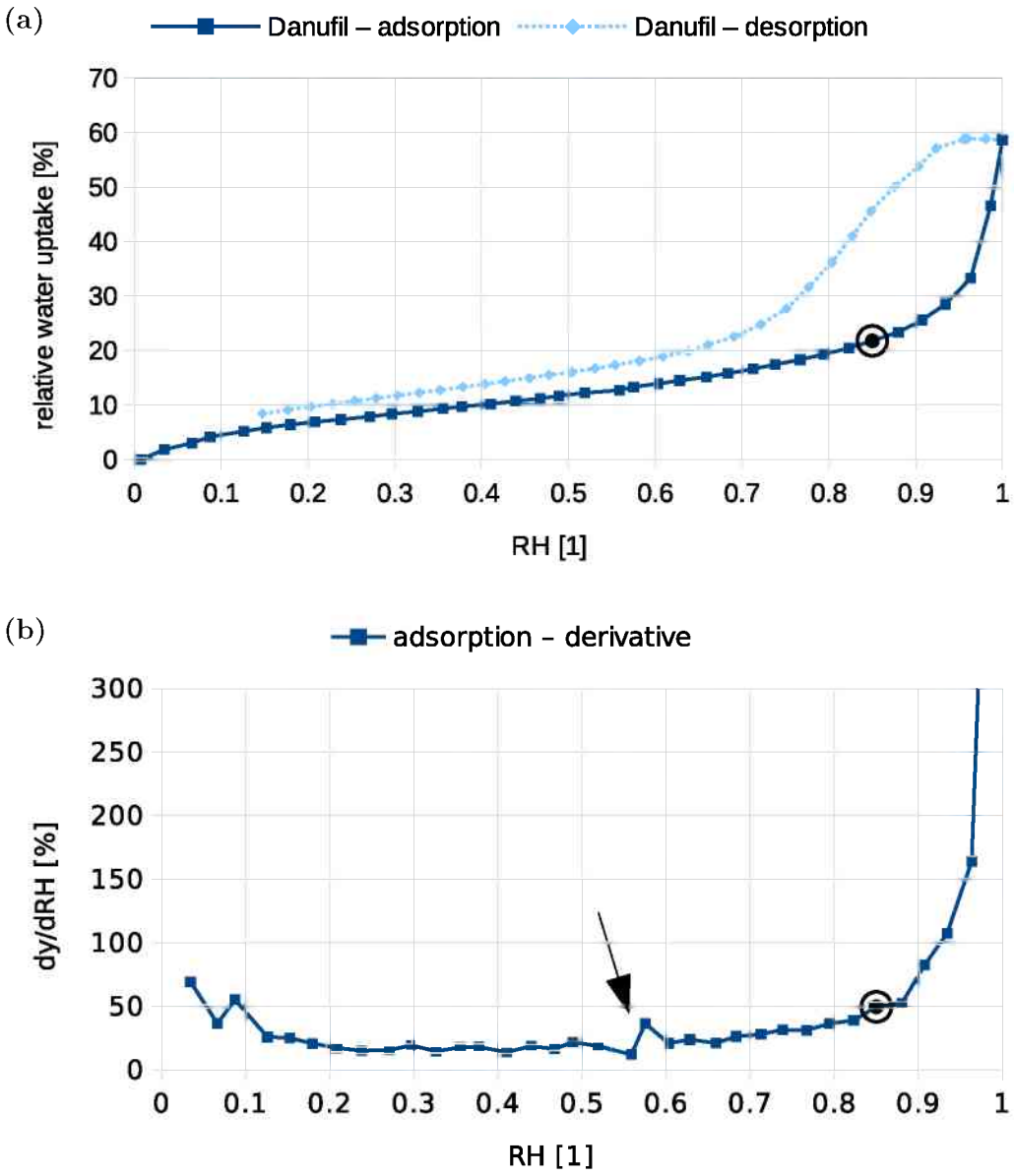

Figure 4.8: (a) Danufil fiber sorption isotherm of the 20 mg series fibers at 17 °C. The mass of the dried fibers was 22.4 mg. (b) Derivative of the adsorption curve.

one looks closely at the horizontal part of the desorption curve, one detects an increase of water uptake. The relative water uptake amounts to 0.85 % and took place in a time frame of three hours. Two reasons can be considered to explain this behavior: a change in the temperature and condensation within the construction, especially near the pressure gauges. Since the effect is small it was deemed negligible. Between the respective parts of the desorption curve, which are associated with micropores and the

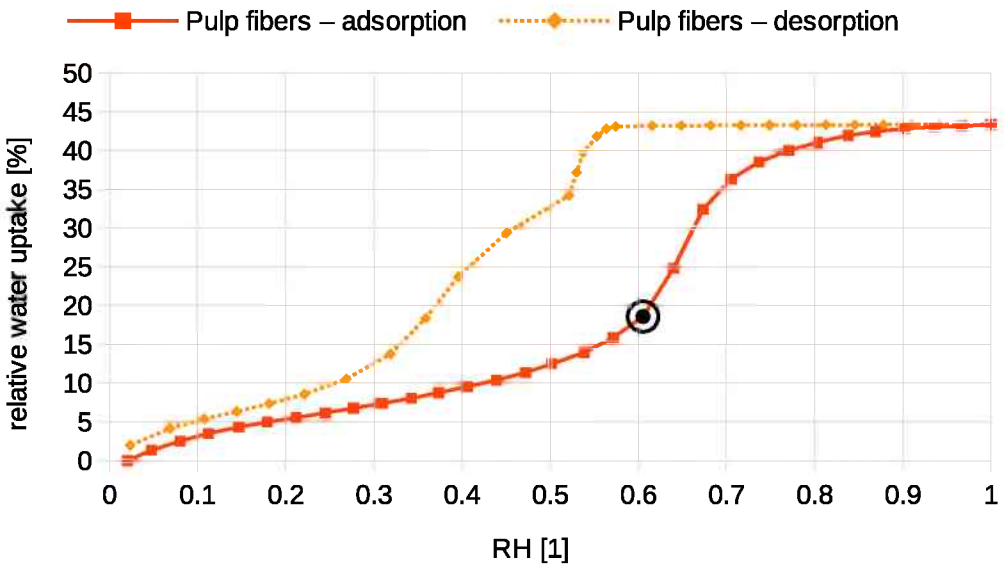

Figure 4.9: Pulp fiber sorption isotherm of the 20 mg series fibers at 17 °C. The mass of the dried fibers was 91.2 mg.

surface with easy accessible macropores, the bigger part of the relative water uptake might be attributed to mesopores. The relative water uptake was determined to be 31 %. The sample mass of the dried fibers was 70.9 mg.

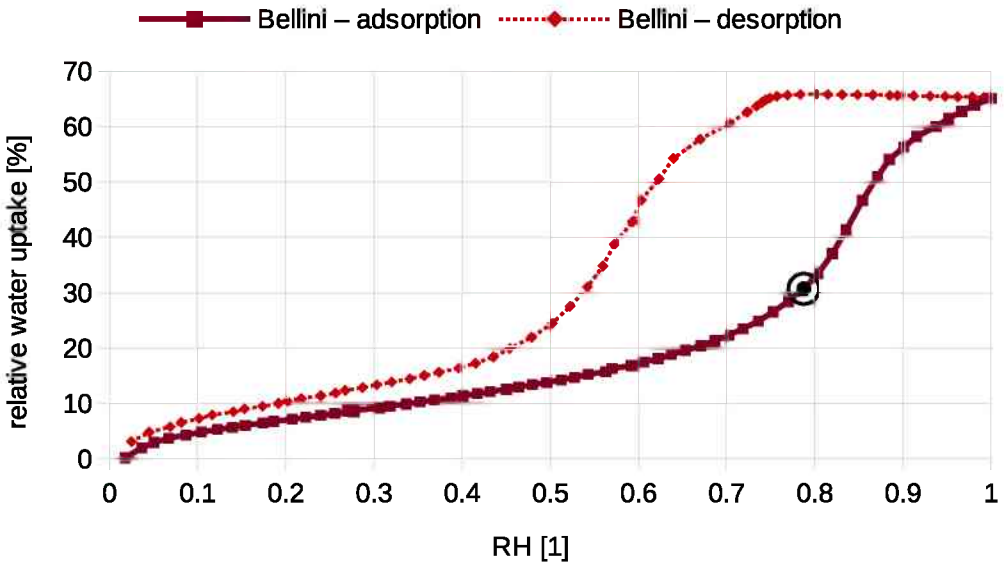

Figure 4.10: Bellini fiber sorption isotherm of the wire cage fibers at 17 °C. The mass of the dried fibers was 70.9 mg

Fig. 4.11 represents the recorded sorption isotherm of Verdi type fibers. The Verdi

fibers in both, the 20 mg series and the wire cage series, resemble the *H4* hysteresis loop. But similar to the Bellini fibers in Fig. 4.10, the desorption curve experiences saturation, which can be seen in the nearly horizontal part at high RH. Considering the difference of density of fibers in both sample configurations, the saturation might be correlated to network behavior. Here too, the horizontal part of the desorption curve experiences a slight increase at decreasing RH. This is also contributed to the aforementioned reasons. But considering the duration for the recording of the adsorption curve - in this case about 25 hours - it is easy to imagine that, when the recording of the desorption curve starts, vapor condenses somewhere within the construction apart from the sample. The relative water uptake was determined to be 33 %.

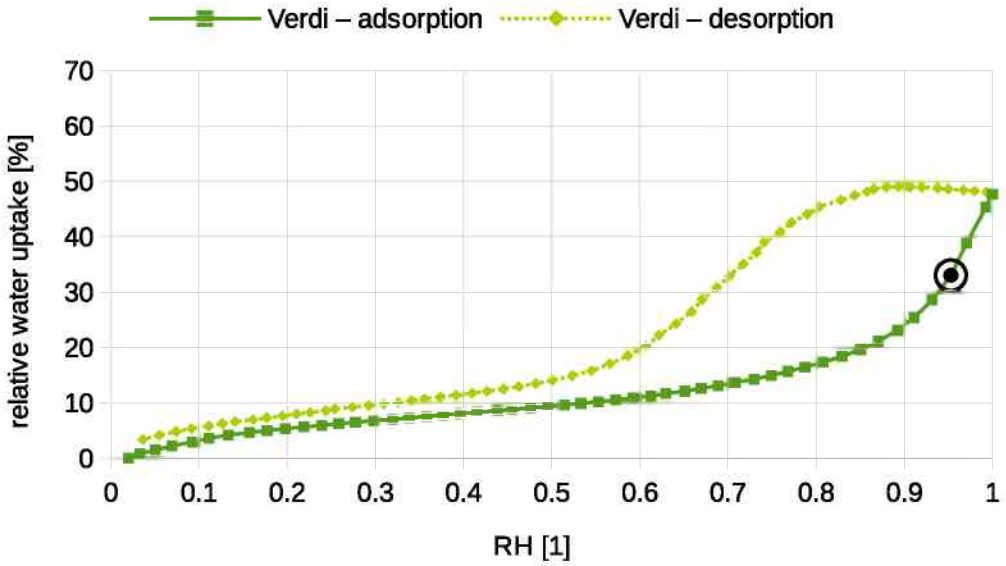

Figure 4.11: Verdi fiber sorption isotherm of the wire cage fibers at 17 °C. The mass of the dried fibers was 121.1 mg.

The isotherms of Fig. 4.12 represents Danufil fibers and Fig. 4.13 represents pulp fibers. Looking at Fig. 4.12 and Fig. 4.13, one notices that both hysteresis loops bear a high resemblance and correspond to the *H2* loop quite well. The curves of both isotherms share even the same features. Both desorption curves exhibit saturation at high RH, followed by a sharp, almost vertical descent, which is likely correlated to easy accessible macropores and the fiber surfaces [19,39,40]. After that follows, what is believed to be the transition to mesopores. This interval is located at $0.50 < RH < 0.69$ for Danufil and at $0.45 < RH < 0.62$ for pulp fibers. The suspected mesopores seem to have the biggest amount of absorbed water. However, the pore network and macropores are also having an effect on the desorption. The section with the presumed mesopores is followed by the transition to micropores. On the other hand, the transition between monolayer and multilayer adsorption is difficult to discern in both isotherms. Also, the filling of the various pore sizes does not lead to visible transition points in the isotherms. This is caused by the interconnection of the pores [19,39,40,42]. Only at high RH, the

adsorption curves reveal two different sections, one with a steep increase, followed by a section where the steep increase lessens until saturation is achieved. The analysis of the sorption isotherms for Danufil fibers and pulp fibers yielded values for the water uptake of 34 % and 26 %, respectively. Please note, that the pulp fibers were already in a densely packed state from the start and did not require a wire cage. Instead, a small chunk of fibers was separated and directly hooked to the microbalance.

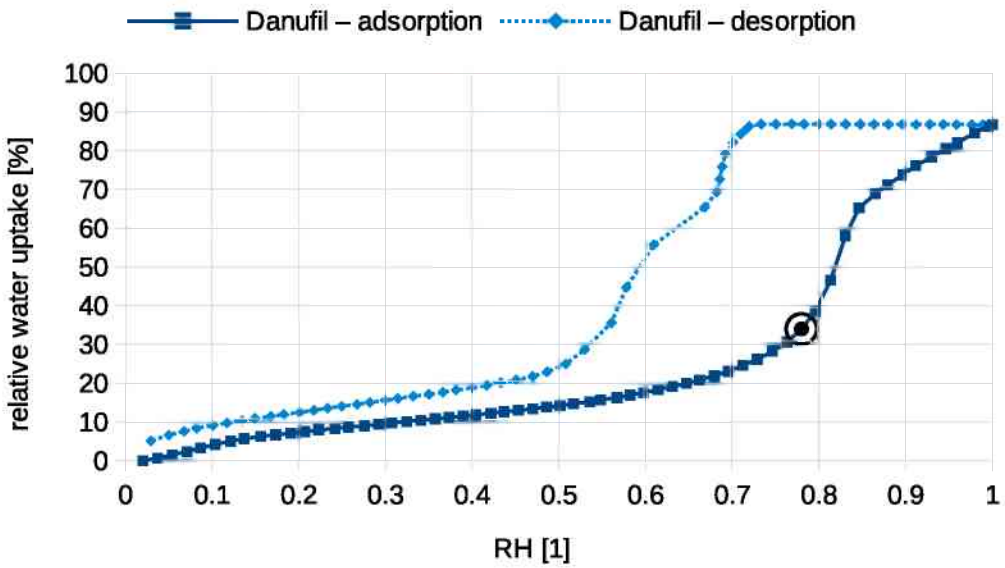

Figure 4.12: Danufil fiber sorption isotherm of the wire cage fibers at 17 °C. The mass of the dried fibers was 16.5 mg.

4.1.3 Summary

The results obtained from the recorded sorption isotherms are presented in Fig. 4.14. The data from the first measurements are close to the results from the 20 mg series. As can be seen, pulp fibers seem to have a lower ability to take up water from vapor than regenerated fibers, regardless of the sample configuration. Also, the water uptake of the viscose fibers in the 20 mg series are all slightly above 20 % and close to each other. On the other hand, the relative water uptake for the viscose fibers in the wire cage series differs more, but are all above 30 %. The differences in the results can be attributed to different sample configuration. For the 20 mg series, loose fiber bundles were prepared, while for the wire cage, the fibers were tightly compacted into a wire cage. In other words, the results from the 20 mg series are believed to correlate to single fiber behavior, while the results from the wire cage series should correlate to network behavior. The combination of high sample mass and densely packed fibers seems to lead to saturation in the hysteresis loops. The long time it takes for the desorption curve from $RH = 1$ to reach the transition to easy accessible macropores and the fiber surface is likely due to network effects between the fibers and the pore

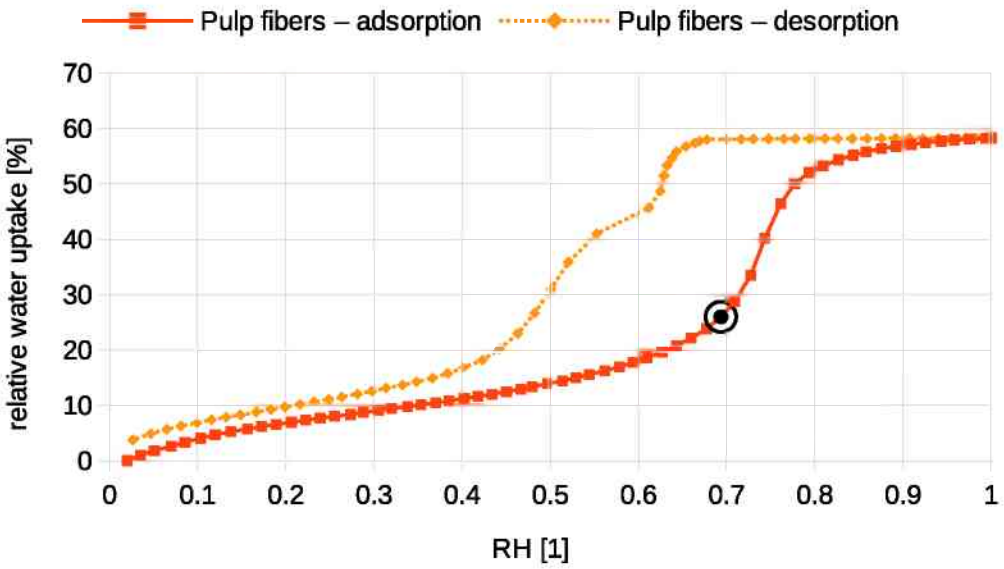

Figure 4.13: Pulp fiber sorption isotherm of the wire cage fibers at 17 °C. The mass of the dried fibers was 33.4 mg.

network holding back the water [42]. But if the fibers are too far from each other, the occurrence of saturation is less probable. Then, the fibers resemble the *H4* loop, like the isotherms of the 20 mg series. *H4* loops are associated with slit-like pores and plate-like agglomerates. The equivalent on the samples of this work are believed to be ripples, perpendicular to the cross-sections of the viscose fiber, presented in Fig. 3.2 of the previous chapter. Those ripples might play a major role for single fiber absorption.

Other works in literature engaged in determination of the pore size and the mechanisms related to pore interconnections [20–22,39,42]. However, these methods are not applicable to sorption isotherms recorded here. Too many factors like multilayer adsorption, a mostly uniform pore size distribution, capillary forces, hydrogen bonding, etc., come into play and interfere with each other. Thus, only a qualitative interpretation of the isotherms was carried out. For better differentiation between each viscose fiber type, more data for statistical analysis is necessary.

4.2 AFM results

In this work, the goal of AFM analysis was to determine relevant topographical influences on the ability of water uptake. Therefore, as displayed in table 3.2 of the previous chapter, two sets of samples taken randomly from different batches were prepared. Their ability for water absorption was tested in the factory prior to delivery. Hence, although randomly taken, it was ensured that each set of samples consisted of fibers with an ability of water absorption above average for the one set and below average for the other set. The random samples of each set have been analyzed and

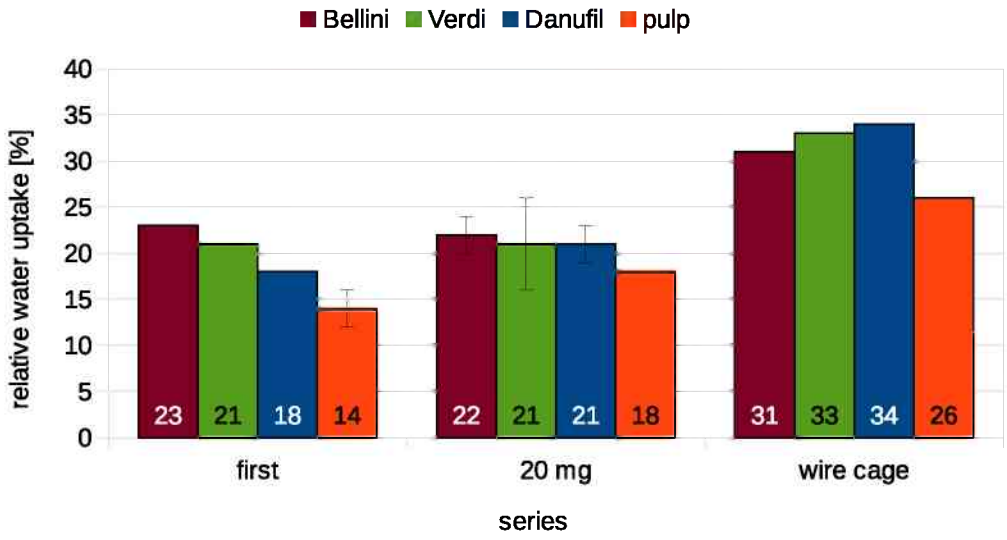

Figure 4.14: Overview of the values for the relative water uptake obtained from the recorded sorption isotherms. The columns with deviations denote averaged results from several recorded isotherms. For Bellini, Verdi, Danufil, and Pulp, respectively, two, five, five, and four results were averaged.

compared to each other. All analyzed samples were trilobal viscose fibers. Some local sites on the viscose fibers displayed a height increase outmatching the available z-range of the AFM in use ($\pm$ 5 μm). Due to the shape of their cross-section - collapsed trilobal fibers - and the resulting high local curvature, the maximum image size was limited to 5 μm $\times$ 5 μm. The chosen scan sites correspond to the flat areas on the viscose fibers. Please note that the results include the curvature of the viscose fibers. Thus, the presented results can be assumed to underestimate the absolute roughness values slightly, due to excluding high curvature areas. After averaging over several AFM images, including the curvature of the fibers, the results should yield topographical roughness parameters, close to reality. Furthermore, the purpose of the results is to compare them relative to each other, including all their topographical peculiarities.

4.2.1 Comprehensive roughness analysis

All AFM images underwent, prior to roughness analysis, step line correction, where adjacent scanlines are aligned to each other, and subtraction of a mean plane. The first measurements showed not only that viscose fibers can differ largely from each other, but even scan sites on the same fiber may display great differences. Therefore, to get a statistical relevant result the roughness was determined from three independent scan areas per fiber. For the following comprehensive roughness analysis, images of each set will be investigated to see if both sets have similar trends with respect to their water absorption. The sets of samples will be referred to as set 1 and set 2.

4.2.1.1 Set 1: GUG-VY6 and GUG-VY8

Set 1 consists of viscose fibers from batch GUG-VY6 with a relative water absorption above average and GUG-VY8 with a relative water absorption below average. Fig. 4.15a displays a 5 μm × 5 μm AFM height image of the sample GUG-VY6 with the roughness parameters $\sigma = 19\ nm$, $\xi = 290\ nm$, and $\alpha = 0.65$, obtained by using the HHCF. Fig. 4.15b displays a 3D-presentation of the surface. As can be seen, the surface experiences almost no curvature or surface impurities. The roughness parameters are below the average values for 5 μm × 5 μm images, presented for GUG-VY6 in table 4.1. The dashed line in Fig. 4.15a represents the orientation of the main fiber axis. The area in the green square marks a high resolution image with scan size of 2 μm × 2 μm presented in Fig. 4.16a in order to further investigate local peculiarities on the surface. This will be dealt within the discussion about the surface morphology. In a similar manner, the green square in Fig. 4.16a is a high-resolution image with a scan size of 1 μm × 1 μm displayed in Fig. 4.16b. The respective values for the RMS-roughness σ are 18 nm and 12 nm. This decrease in σ with the scan size can usually be explained by a smaller influence of the curvature on a smaller scan site, as well, as a smaller influence of big surface features on a smaller scan site.

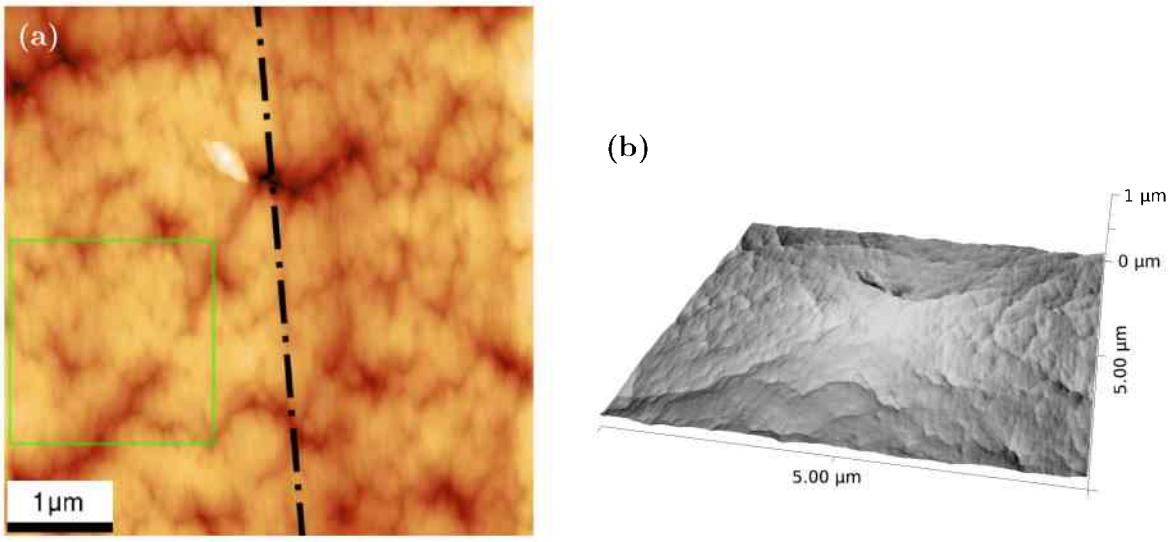

Figure 4.15: (a) 5 μm × 5 μm AFM height image of GUG-VY6, z-scale: 220 nm. The green square marks the position of a 2 μm × 2 μm image in Fig. 4.16a. The black line represents the orientation of the main fiber axis. (b) 3D-visualization of the same surface area.

The 5 μm × 5 μm AFM height image presented in Fig. 4.17a is also obtained from a fiber of GUG-VY6. The values for the obtained roughness parameters σ, ξ, and α are 114 nm, 800 nm, and 0.70, respectively. Compared to values of Fig. 4.15a, the roughness parameters are larger. Actually, σ and ξ are above the average values for GUG-VY6 presented in table 4.1. By comparing Fig. 4.17 and Fig. 4.15, the aforementioned differences within fibers, produced in the same batch, become obvious. The number of

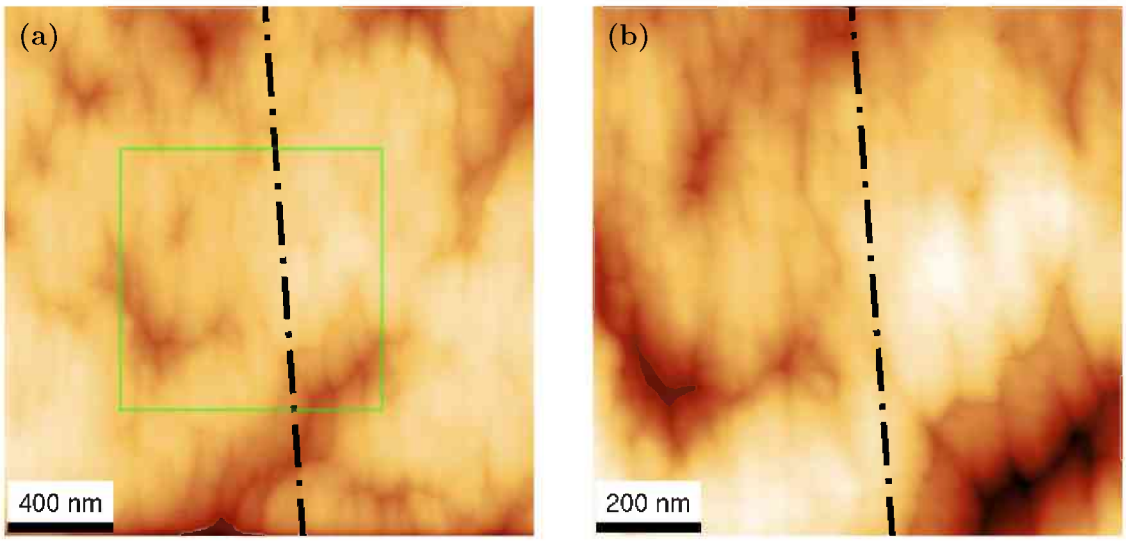

Figure 4.16: (a) 2 μm × 2 μm AFM height image of GUG-VY6, z-scale: 170 nm. The green square marks the position of a 1 μm × 1 μm AFM height image, z-scale: 70 nm, presented in (b). The black lines represent the orientation of the main fiber axis.

surface features seems to be less. This is also supported by the higher lateral correlation length ξ. On the other hand, viewing Fig. 4.17b it is clear that the curvature has the main influence on σ. After flattening the surface, by subtracting a polynomial background of the 5th order, σ changes from 114 nm to 18 nm, a value approximately 6 times smaller and in the same range as σ for Fig. 4.15. The polynomial background subtraction and the recalculation of σ was performed using Gwyddion.

Please be reminded that the goal of these measurements is to compare the batches of sample sets relatively to each other, with correlation to their ability of water absorption - in this case, trilobal fibers from set 1 consisting of fibers from the batches GUG-VY6 and GUG-VY8. In order to incorporate all available surface information, the final results of the roughness analysis **will include** curvature and surface features.

Fig. 4.18a represents a 5 μm × 5 μm AFM height image of GUG-VY8. The respective roughness parameters σ, ξ, and α, according to the analysis of the HHCF, are 163 nm, 750 nm, and 0.8. In the bottom right corner of the image, an elevated area, suspected to be a surface impurity, can be observed. Fig. 4.18b, represents a 3D-visualization of the surface, where the curvature of the fiber is better displayed. Different from Fig. 4.17b, here, the right edge of Fig. 4.18b is bent upward, further increasing the value of σ. Again, subtracting a polynomial background of the 5th order and further excluding the suspected surface impurity with a mask, σ changes from 163 nm to 18 nm - an approximately 9 times smaller value. Without masking the surface impurity, σ becomes 23 nm.

For comparison, another 5 μm × 5 μm image (Fig. 4.19a) of GUG-VY8 is presented. The analysis of the roughness yielded for σ, ξ, and α are 28 nm, 320 nm, and 0.60, respectively. On the surface, a higher density of surface features can be observed, com-

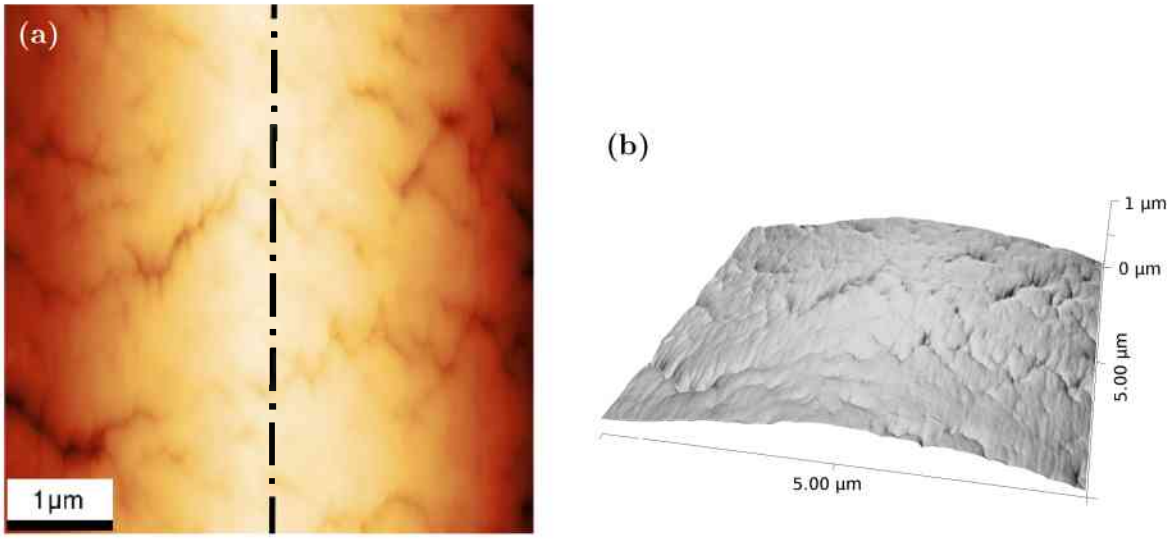

Figure 4.17: (a) 5 μm × 5 μm AFM height image of GUG-VY6, z-scale: 500 nm. The black line indicates the orientation of the main fiber axis. (b) 3D-visualization of the same surface area.

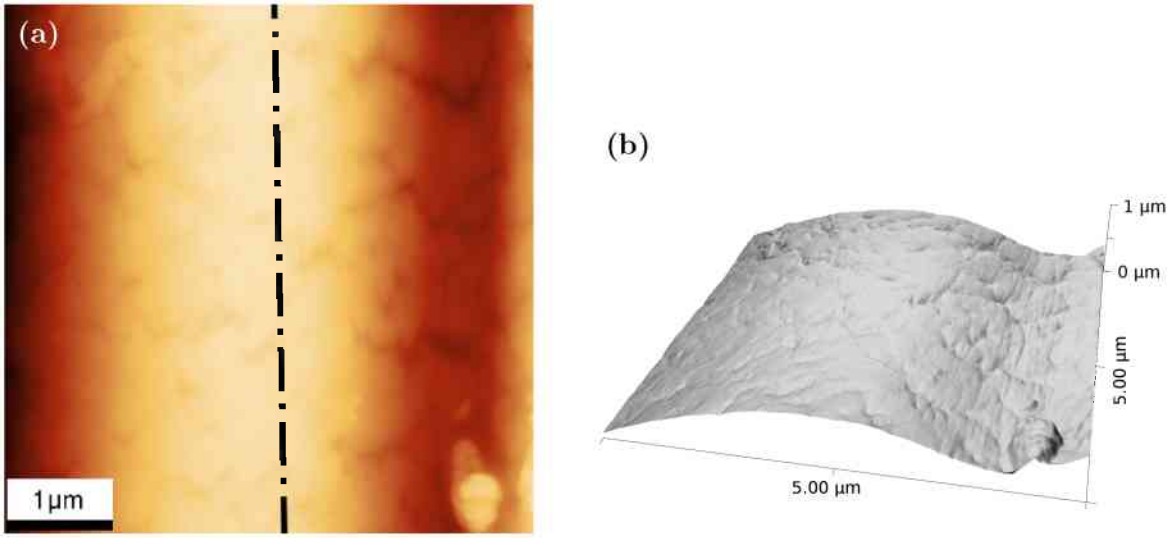

Figure 4.18: (a) 5 μm × 5 μm AFM height image of GUG-VY8, z-scale: 700 nm. The black line represents the orientation of the main fiber axis. (b) 3D-visualization of the same surface area.

pared to Fig. 4.18a. This corresponds to the smaller value of ξ, which is actually about two times smaller. There is almost no curvature resulting in a smaller σ. Still, after subtracting a polynomial background of the 5th order σ yields 19 nm. On the surface in Fig. 4.19, ripples almost parallel to the main fiber axis with an average distance of 100 nm to 200 nm to each other can be observed. This gives the optical impression of a jagged surface, which might correlate to the smaller value for α, compared to Fig. 4.18. The ripples originate likely from solidifying after wet spinning and are of varying dis-

tances to each other. When the interior of the viscose fiber solidifies and loses humidity, contraction occurs and the already solid surface forms ripples.

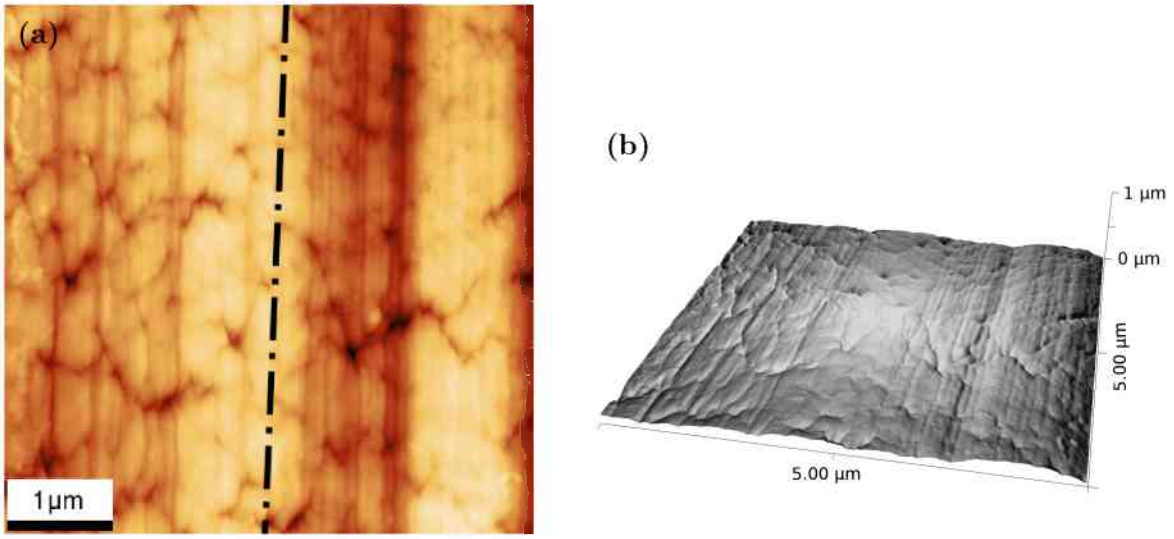

Figure 4.19: (a) 5 μm × 5 μm AFM height image of GUG-VY8, z-scale: 180 nm. The black line represents the orientation of the main fiber axis. (b) 3D-visualization of the same surface area.

For the topographical analysis of set 1, twelve AFM images of GUG-VY6 and 10 AFM images of GUG-VY8 were recorded. The resulting averaged roughness parameters are presented in table 4.1. Comparing both average values for σ reveals that their average values are the same, only their deviation differs. Also, the corresponding values for α are very close. Only the average values for the lateral correlation length ξ show some difference. However, given the deviation the difference in ξ is insignificant.

4.2.1.2 Set 2: VY-384002 and VY-384749

Set 2 consists of the viscose fibers VY-384002 with a relative water absorption below average and VY-384749 with a relative water absorption above average. Fig. 4.20a represents a 5 μm × 5 μm AFM height image of VY-384002. The respective roughness parameters σ, ξ, and α are 35 nm, 410 nm, and 0.70. Ripples, parallel to the main fiber axis, can be observed. Also, the slight curvature forms a wave pattern with its wave peaks aligned almost parallel to the main fiber axis. Near the left top corner and on the right edge of the image, elevated areas, appearing nearly white, are visible to the eye. After subtracting a polynomial background of the 5th order and masking the elevated areas, which are suspected of being surface impurities, like particles or dust, σ changes from 35 nm to 14 nm. Without the mask, σ is 21 nm.

For comparison with Fig. 4.20a, a 5 μm × 5 μm AFM height image in Fig. 4.21a is presented. The roughness parameters σ, ξ, and α are 140 nm, 580 nm, and 0.60, respectively. Interestingly, here, the surface morphology does not align with the main fiber axis - neither the curvature nor the ripples. This can be explained by the sample

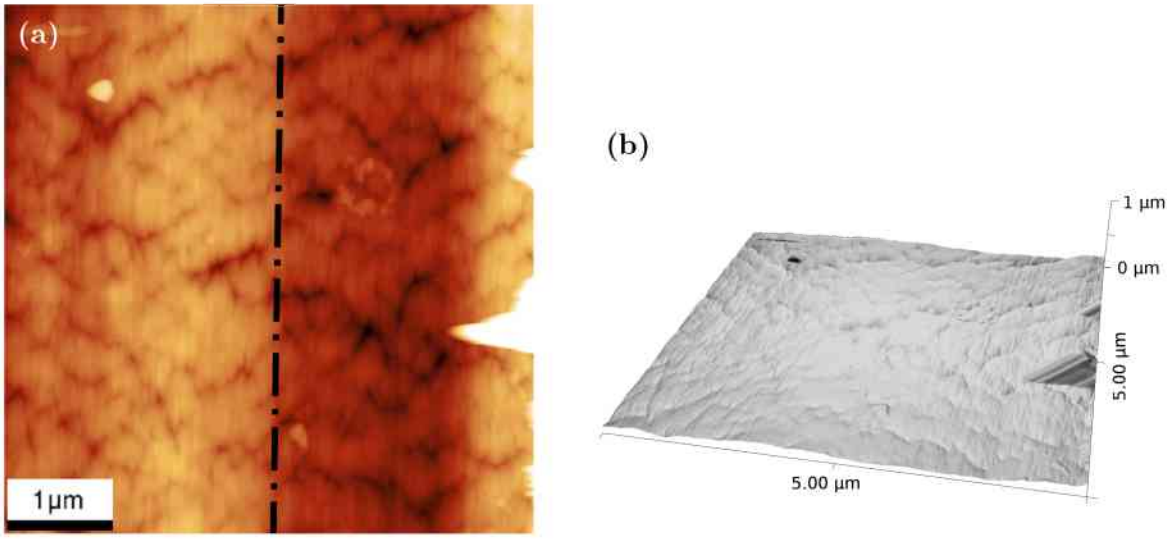

Figure 4.20: (a) 5 μm × 5 μm AFM height image of VY-384002, z-scale: 200 nm. The black line represents the orientation of the main fiber axis. (b) 3D-visualization of the same surface area.

mounting. The reason for this peculiarity can be observed in a few OM, where the torsion of the viscose fiber is visible. In this case, the fiber is rotated counterclockwise, according to the orientation of the main fiber axis in Fig. 4.21a. In the bottom center of Fig. 4.21a, represented by brighter colors, a surface impurity can be easily distinguished from the surface, due to its shape. The bottom half of the left edge bends upwards, looking like a crease. Considering the cross-section of the fiber, this is very likely a site, where a trilobal leg branches off. After masking the surface impurity and the crease, followed by polynomial background subtraction of the 5th order, σ changed from 140 nm to 17 nm. Including the masked areas, σ yields 107 nm. Including the crease, with only the surface impurity masked, σ yields 106 nm. Thus, as expected, the crease is the main contributor to the RMS-roughness, surpassing curvature and surface impurities. In Fig. 4.21 there are less surface features than in Fig. 4.20, corresponding to the higher value for ξ. The α value is rather surprising. The surface on Fig. 4.21 looks smoother and one would expect a higher value for α compared to Fig. 4.20, which is not the case. This phenomenon might be correlated to the crease in Fig. 4.21.

Fig. 4.22a shows a 5 μm × 5 μm AFM height image of VY-3844749. The analysis of the HHCF yielded for the roughness parameters σ, ξ, and α, respectively, 77 nm, 800 nm, and 0.70. Again ripples, nearly parallel to the main fiber axis, are visible. In the bottom left a surface impurity is located. The slight curvature of the surface forms a shallow valley. After masking the surface impurity and subtracting a polynomial background of the 5th order, σ changes from 77 nm to 13 nm, about 6 times smaller. Including the impurity, σ yields 15 nm.

For comparison, Fig. 4.23a represents a 5 μm × 5 μm AFM height image of VY-3844749, as well. The respective roughness parameters σ, ξ, and α are 212 nm, 550 nm, and 0.7. The shape of the surface resembles a bar stool, with the wave peaks of its

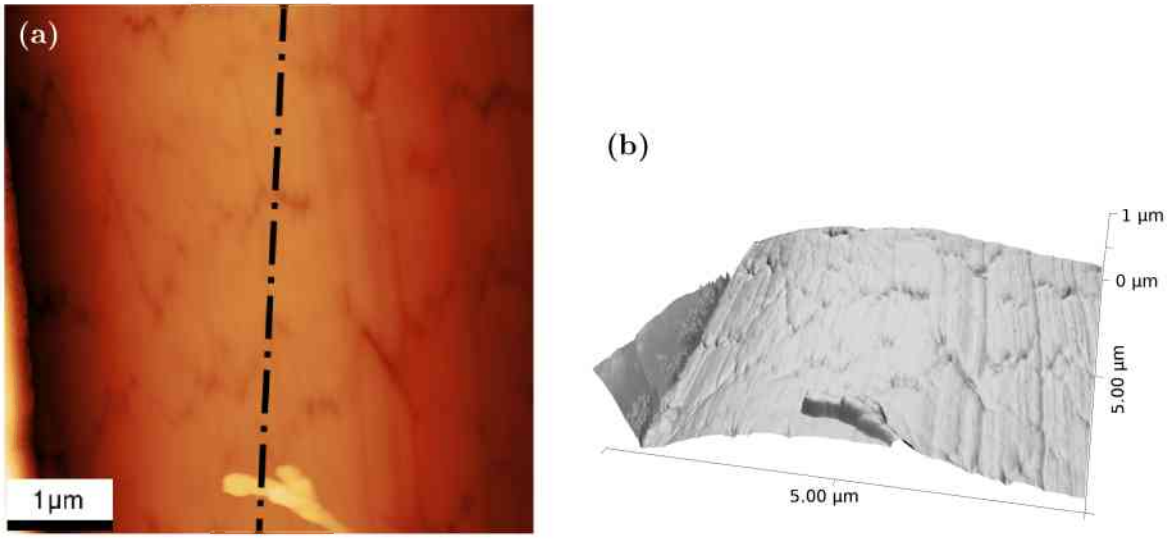

Figure 4.21: (a) 5 μm × 5 μm AFM height image of VY-384002, z-scale: 1 μm. The black line represents the orientation of the main fiber axis. (b) 3D-visualization of the same surface area.

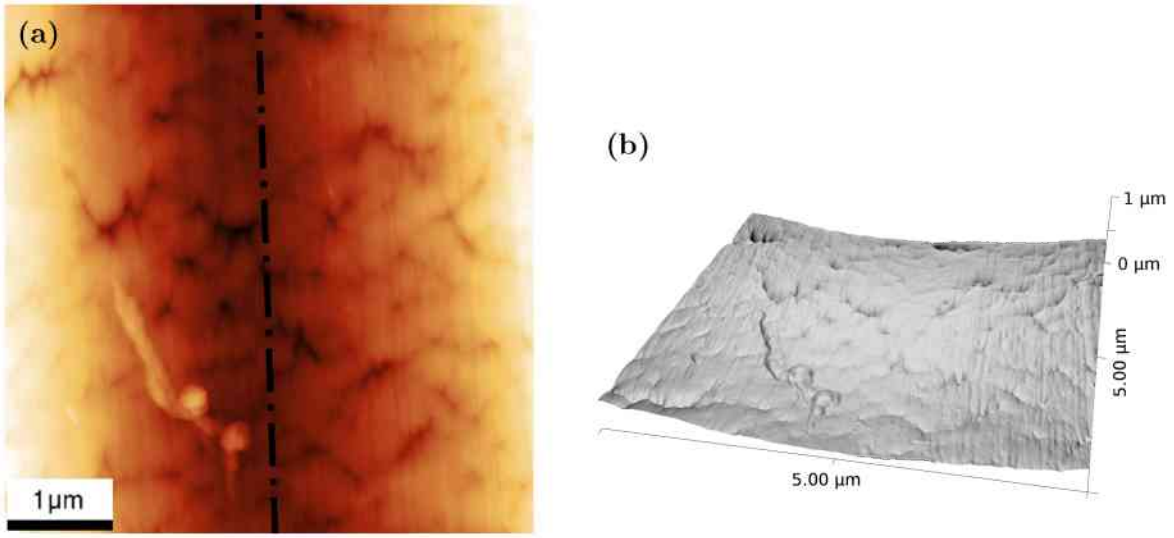

Figure 4.22: (a) 5 μm × 5 μm AFM height image of VY-384749, z-scale: 350 nm. The black line represents the orientation of the main fiber axis. (b) 3D-visualization of the same surface area.

wave pattern aligned nearly parallel to the main fiber axis. Ripples, almost parallel to the fiber axis, are visible near the center of the image. The RMS-roughness is higher compared to Fig. 4.22. This can be attributed to the curvature, especially to the crease on the right edge of the AFM image. The crease very likely indicates the branching off of the trilobal legs of the viscose fiber. After subtracting a polynomial background of the 5th order, σ yields 33 nm - about two times higher than the surface of Fig. 4.22 after polynomial subtraction. The number and size - in lateral direction, as well as

in z-direction - of the surface impurities is negligible. The density of surface features correlates with the lower value of ξ compared to Fig. 4.22. One would expect α to be higher for the surface of Fig. 4.22, due to the numerous ripples on the left and right edges of the AFM image, but both Hurst parameters have actually the same value. The influence of the ripples on the jaggedness of the surface is thus rather small.

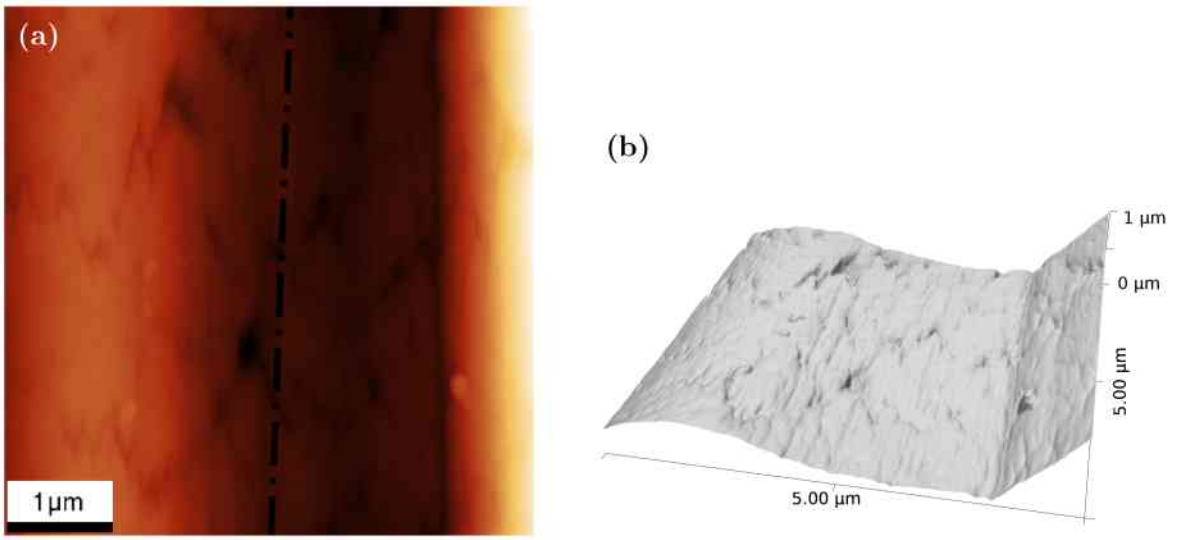

Figure 4.23: (a) 5 μm × 5 μm AFM height image of VY-384749, z-scale: 1.1 μm. The black line represents the orientation of the main fiber axis. (b) 3D-visualization of the same surface area.

For the topographical analysis of set 2, 10 AFM images of VY-384002 and 10 AFM images of VY-384749 were recorded. The resulting averaged roughness parameters are presented in table 4.1. The comparison of the σ values shows a distinct difference, with VY-384749 having the higher RMS-roughness. With the high deviation for ξ, however, their different average values become insignificant. Also the average values and deviations of α are too close to determine any significant differences.

4.2.1.3 Summary

The results of the comprehensive roughness analysis with the parameters σ, ξ, and α for both sample sets, including two batches per set, are presented in table 4.1. The results presented were obtained by analyzing and fitting the HHCF. The results include the curvature of the fibers and the surface impurities, where the curvature has a huge impact on RMS-roughness while the surface impurities are negligible. The reason for this decision was to compare the viscose fiber surfaces as a whole to each other. The RMS-roughness of 5 μm × 5 μm areas after subtracting a polynomial background are relatively small and the resulting values for σ are close to each other. Table 4.2 shows the RMS-roughness for the same AFM images after a polynomial subtraction of the 5th degree and masking the surface impurities. Here, it can be seen that the flattened surfaces display an at least three times smaller RMS-roughness than in table 4.1.

Furthermore, the values for σ in a set are very close to each other. Differences might be found in the curvature. By averaging the obtained data, including curvature and surface impurities, the results should yield information about the true surface of the fiber.

Either due to close average values or too large deviations, no distinct differences for σ, ξ, and α could be found, as can be seen in table 4.1. Similar trends for ξ and α are distorted by either too large deviations or too close average values. The only exceptions are the values for RMS-roughness of VY-384002 and VY-384749. σ for VY-384749 is about three times larger than σ for VY-384002 and even considering their respective deviations, the difference is distinct. Incidentally, VY-384749 being the batch with the water absorption above average. This would support the intuitive thought of a high surface roughness leading to more surface area, which leads to better water uptake. On the other hand the same must be true for the other set with GUG-VY6 and GUG-VY8. However, this is not the case. Thus, it can be concluded that the roughness parameters of the viscose fibers are not the reason for the different abilities in water uptake.

Table 4.1: Comparison of the roughness parameters obtained from 5 μm × 5 μm AFM images for both sample sets using the HHCF. The influence of the curvature and surface features on the obtained results is included. The indication in the brackets denotes the deviation in percent.

sample	water absorption	σ nm	ξ nm	α 1
GUG-VY6	high	58 ± 25 (43 %)	620 ± 140 (23 %)	0.70 ± 0.05 (7 %)
GUG-VY8	low	58 ± 40 (69 %)	560 ± 160 (29 %)	0.65 ± 0.10 (15 %)
VY-384002	low	54 ± 31 (57 %)	530 ± 180 (34 %)	0.65 ± 0.10 (15 %)
VY-384749	high	146 ± 47 (32 %)	650 ± 100 (16 %)	0.70 ± 0.10 (14 %)

Table 4.2: Comparison of the RMS-roughness obtained from 5 μm × 5 μm AFM images after a polynomial background subtraction of the 5th degree and masking of the surface impurities.

sample	water absorption	σ nm
GUG-VY6	high	16 ± 1 (6 %)
GUG-VY8	low	15 ± 3 (20 %)
VY-384002	low	19 ± 7 (39 %)
VY-384749	high	19 ± 5 (28 %)

4.2.2 Surface morphology

Aside from the occasional impurities, trenches were detected on the surface. The trenches can be generally identified as the dark structures on the surfaces of the AFM images. They probably formed during solidification after wet spinning, e.g. stretching of the fibers. Comparing several images, it is obvious that these trenches are the major feature on the fiber surfaces. Thus, their detailed analysis is of great interest.

Fig.4.24a represents a 5 μm $\times$ 5 μm AFM height image of a GUG-VY8 fiber. The dashed line represents the main fiber axis orientation. The inset in the top right corner is the FFT of the topography image. In the FFT diagram, the sharp horizontal chain of dots, indicated by a green arrow, corresponds to the aforementioned ripples. The ellipsoid shape of the white dots, indicated by another green arrow, corresponds to the high surface feature on the AFM image (with their orientations of dots in the FFT nearly being perpendicular to each other). This elevated area is most likely a surface impurity or surface feature of the fiber. From this, it can be seen that the surface impurity has a strong influence on the FFT image. Fig.4.24b presents the same surface area, but after a polynomial background subtraction of the 5th order. It can be seen that the trenches are more distinguishable for the manual trench count after the background subtraction. Here, the manual count amounted to 107 trenches. Fig.4.24c represents the same surface area, but this time processed by a MATLAB script. The MATLAB script marks the trenches in red and surface impurities in blue and yielded 87 trenches.

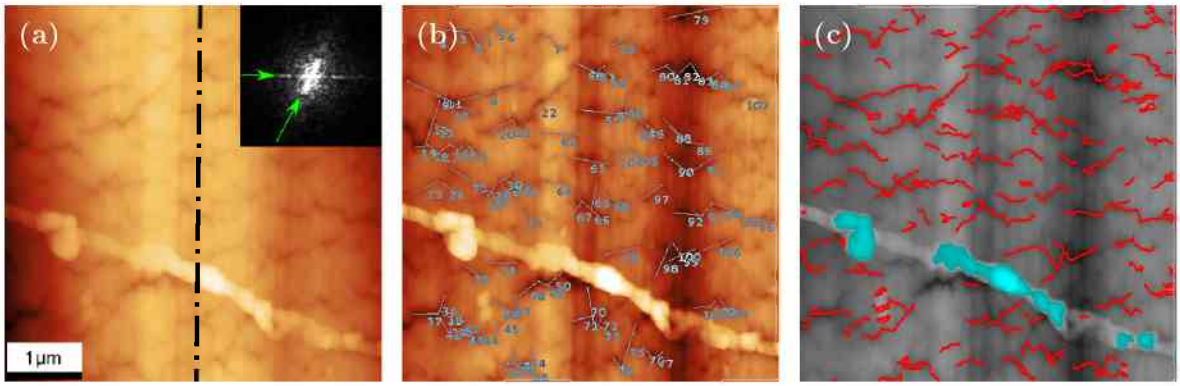

Figure 4.24: (a) 5 μm $\times$ 5 μm AFM height image of GUG-VY8, z-scale: 450 nm. The black line represents the orientation of the main fiber axis. The inset presents an FFT of the AFM image. For the meaning of the green arrows, see text. (b) Manual trench count (107 trenches) after polynomial background subtraction of the 5th order. (c) MATLAB computed trench analysis (87 trenches).

In a similar manner, Fig.4.25a represents a 5 μm $\times$ 5 μm AFM height image from the GUG-VY8 batch. Again, the surface ripples parallel to the main fiber axis result in the sharp chain of dots, indicated by a green arrow, in the FFT inset. Additionally, two more preferential orientations of dots, marked by two green arrows, are visible in the

inset. They correspond to the trench orientations. The surface impurities do not seem to have any relevant influence on the FFT result. The manual trench count presented in Fig.4.25b yielded 82 trenches and the MATLAB script in Fig.4.25c amounted to 84 trenches.

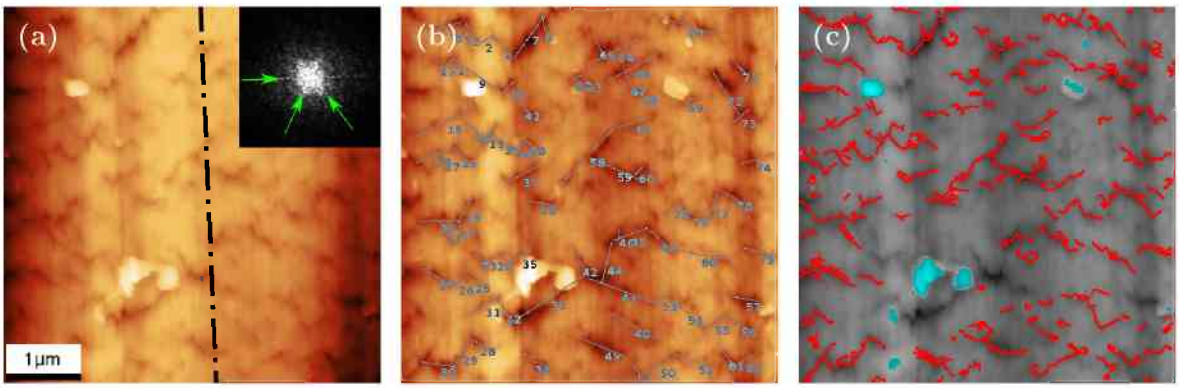

Figure 4.25: (a) 5 μm × 5 μm AFM height image of GUG-VY8, z-scale: 280 nm. The black line represents the orientation of the main fiber axis. The inset presents an FFT of the AFM image. For the meaning of the green arrows, see text. (b) Manual trench count (82 trenches) after polynomial background subtraction of the 5th order. (c) MATLAB computed trench analysis (84 trenches).

Fig.4.26a represents a 5 μm × 5 μm AFM height image of a viscose fiber taken from VY-384002. On the top right corner and in the bottom center, surface impurities, according to the areas marked in blue in Fig.4.26c, can be observed. This time, no sharp horizontal chain of dots is observed in the FFT, however, an orientation parallel to the main fiber axis - perpendicular to the main fiber axis in the FFT - is observed and marked by a green arrow. This might have been caused by the influence of the surface impurity on the top right and the thermal drift in the top edge of the AFM image. The manual and automated trench analysis resulted in 117 and 80 trenches, respectively.

Each trench detected by the manual count was marked by a straight line in the direction of the trench. Based on these straight lines, data of trench orientation and trench lengths were collected as well. The angles of the trenches with respect to the main fiber axis were classified according to Fig. 4.27. With the main fiber axis as base line, representing 0°, angles in clockwise direction from the main fiber axis were signed negative. Angles in counterclockwise direction were signed positive, resulting in angle range from -90° to +90°.

Fig. 4.28 is a presentation of the trench angle distributions by the manual counting of GUG-VY8 (blue bars) and GUG-VY6 (red bars). Each bar on the histogram stands for an angle range of 10°, starting with the first bar from -90° to -80° and ending with the last bar with a range from +80° to +90°. The trench angle distribution for both batches of sample set 1 displays a bimodal distribution. GUG-VY6 might even experience a trimodal distribution near -90° and +90°. While this might be the case, it is obvious to

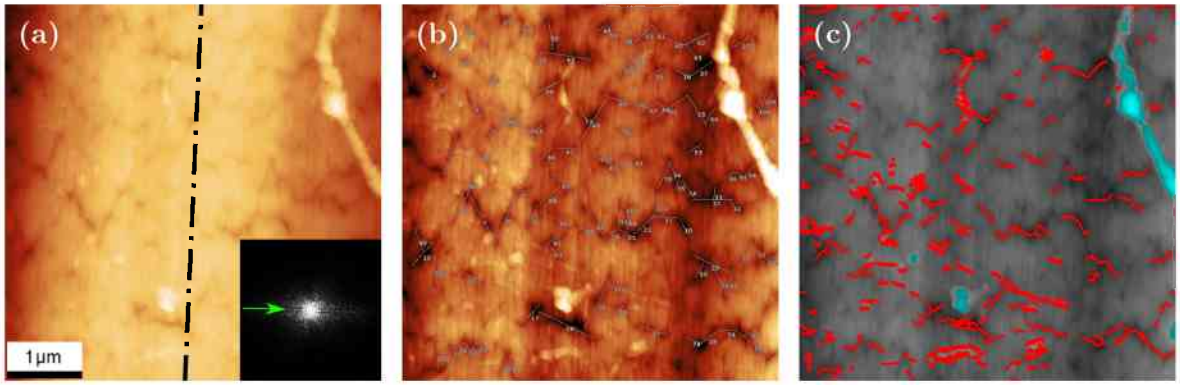

Figure 4.26: (a) 5 μm × 5 μm AFM height image of VY-384002, z-scale: 350 nm. The resolution is 1024×1024 px instead of the usual 512×512 px. The black line represents the orientation of the main fiber axis. The inset presents an FFT of the AFM image. For the meaning of the green arrow, see text. (b) Manual trench count (117 trenches) after polynomial background subtraction of the 5th order. (c) MATLAB computed trench analysis (80 trenches).

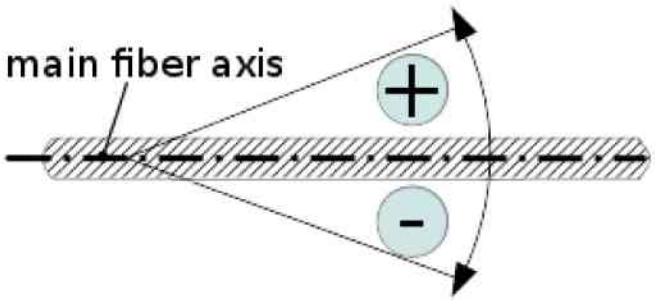

Figure 4.27: Classification of the trench orientation with respect to the main fiber axis. The main fiber axis represents 0°. Trenches aligned in clockwise direction are signed negative and trenches aligned in counterclockwise direction are signed positive. The angle range is limited between -90° and +90°.

the naked eye that the peaks of both distributions are incongruent. The distribution of GUG-VY8 is slightly broader, compared to the two central main peaks of GUG-VY6. It can also be recognized that the number of trenches differs for both sets notably, with GUG-VY8 having 551 trenches, which outnumbers GUG-VY6 with only 245 trenches.

In the same manner, Fig.4.29 represents the trench angle distribution of VY-384002 (blue bars) and VY-384748 (red bars). This time, both data sets clearly exhibit bimodal distributions, with their peak positions relatively close to each other, compared to set 1. The peaks of VY-384749 are slightly shifted to higher angles (10° - 20°), though. Here too, the counted number of trenches differs with VY-384002 having 565 trenches and VY-384749 having 401 trenches.

The trench length distribution of set 1 is presented in Fig.4.30. Both batches follow a log-normal distribution, the peak position of GUG-VY6 as well as the peak position

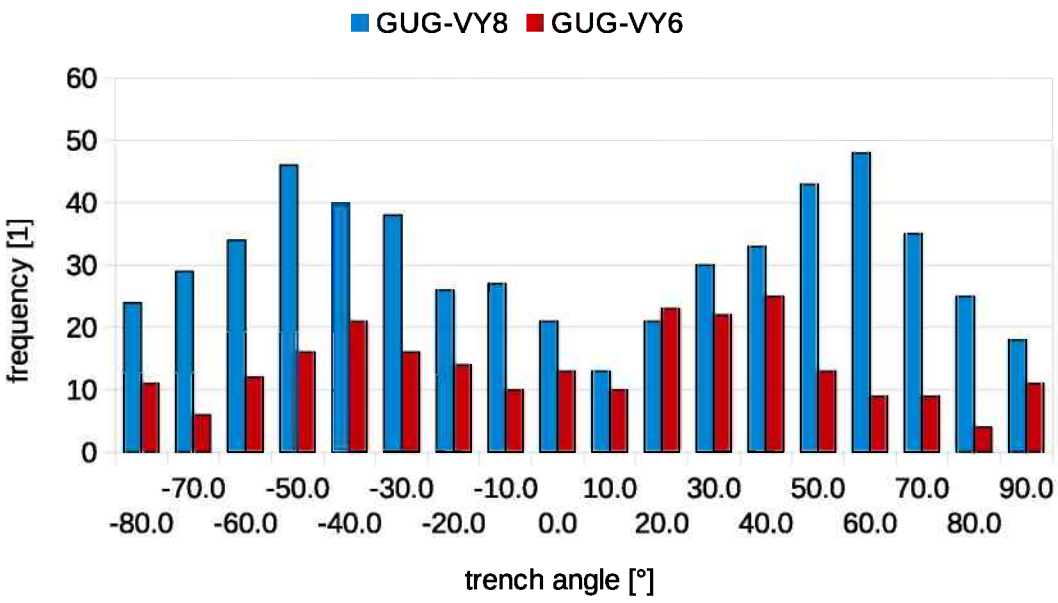

Figure 4.28: Histogram of the trench orientation distribution of set 1. The blue bars denote GUG-VY8 and the red bars denote GUG-VY6. Each bar depicts a range of 10°. The first bar represents a range from -90° to -80°.

of GUG-VY8 are found at 0.3 μm. It also seems that the portion of longer trenches is greater with GUG-VY6, considering the difference in the overall numbers of trenches. Similar to this, Fig.4.31 presents the trench length distribution of set 2. In contrast to the histogram in Fig.4.30, the two trench length histograms in Fig.4.31 resemble each other more closely. Both sets appear to be similar to a log-normal distribution and match each other quite well.

Additionally, it was attempted to characterize the trenches regarding their depths. The problem was that the depth of a single trench differs greatly over its length. Therefore, the trench depth was measured at random positions. Furthermore, only a few representative trenches per AFM image were analyzed. The resulting histogram for set 1 is presented in Fig. 4.32. For GUG-VY8 an amount of 37 trenches and for GUG-VY6 an amount of 25 trenches were measured. The deepest trenches, for both batches, reach about 80 nm in depth. Shallow trenches are hard to detect, thus, the histogram lacks data for those. Considering the difference in total data, both distributions match quite well. Due to the results of set 1 not yielding useful information, a trench depth characterization of set 2 was not attempted.

4.2.2.1 Summary

The analysis of the surface morphology made clear that the main features on the investigated viscose fiber surfaces are surface impurities, trenches, ripples aligned parallel to the main fiber axis, and the curvature that is also aligned parallel to the main fiber

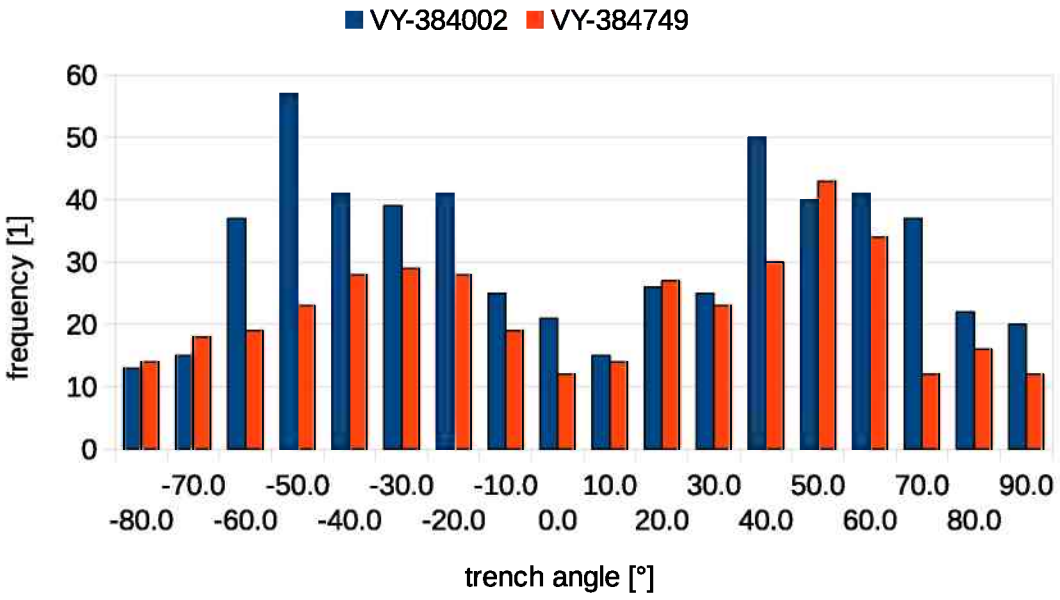

Figure 4.29: Histogram of the trench orientation distribution of set 2. The blue bars denote VY-384002 and the red bars denote VY-384749. Each bar depicts a range of 10°. The first bar represents a range from -90° to -80°.

axis. The surface impurities occur randomly on the surface and do not follow trends depending on which sample they are. The ripples and the curvature can be observed on almost all surfaces of the samples. The ripples as well as the curvature change even within the same AFM image, but follow in general the same trend in aligning themselves parallel to the main fiber axis. The most peculiar surface features are the trenches. The trench density correlates with the lateral correlation length ξ in the roughness analysis. In analogy, the results of the automated trench count, presented in table 4.3, show a similar trend. In both sample sets, the batches with water absorption above average have two common qualities, higher average values for ξ and lower trench densities. The trend for ξ is not reliable, due to the high deviation. The correlation between trench density and ability for water absorption was evaluated statistically. For set 1, the average values show a significant difference according to Welch's test [43] for unequal variances, with a significance level of 0.05. Set 2 shows according to Welch's test a significant difference only for a significance level of 0.20, which can be considered unreliable. The analysis of the trench orientations with respect to the main fiber axis disclosed their inclination towards bimodal distributions, but no correlation with regard to their water absorption properties could be revealed. Likewise, the trench length distribution, which inclined towards a log-normal distribution, and the trench depth distribution do also not correlate with the water absorption capacity.

Take note that for the manual count for each batch of both sample sets, data of five AFM images was analyzed. After the analysis of the manual counts, more data regarding trench density turned into the focus of interest. At this point, the MATLAB

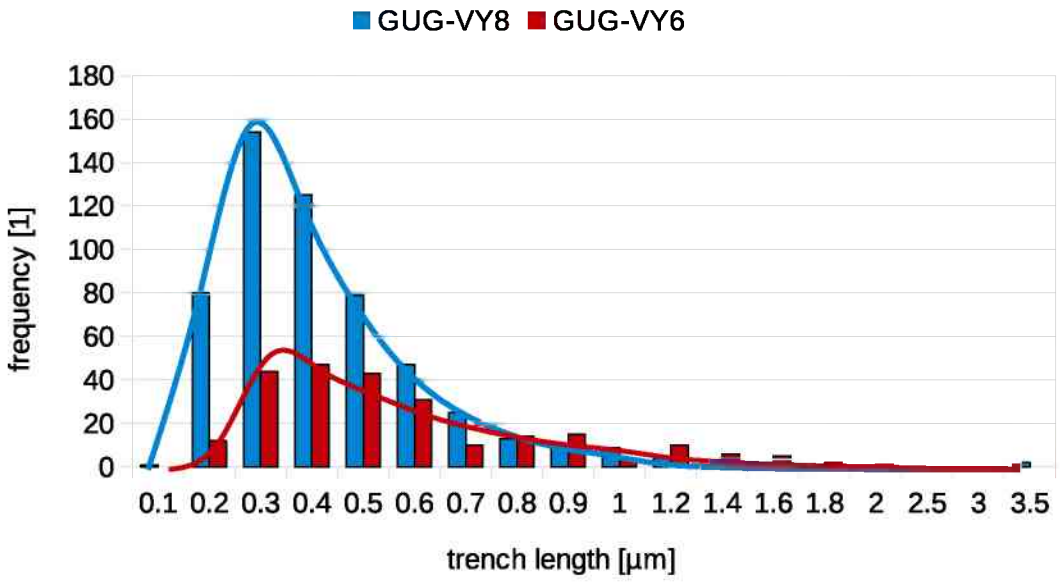

Figure 4.30: Histogram of the trench length distribution of set 1. The blue bars denote GUG-VY8 and the red bars denote GUG-VY6. The fits of the log-normal distribution are indicated by the solid lines.

script for automated trench count came into use, and the number of AFM images increased to its current state, as is presented in table 4.3. All analyzed AFM images were 5 μm × 5 μm in size. While an analysis of 2 μm × 2 μm and 1 μm × 1 μm images was also done, the results yielded no useful data, since the image size was insufficient to capture long trenches.

Table 4.3: Comparison of the average number of trenches N_t obtained from $5\mu m \times 5\mu m$ AFM images for both sample sets using the MATLAB script.

sample	N_t	number of images	water absorption	scale
GUG-VY6	55.3 ± 5.4	12	high	5 μm × 5 μm
GUG-VY8	79.8 ± 6.1	10	low	5 μm × 5 μm
VY-384002	71.6 ± 9.4	10	low	5 μm × 5 μm
VY-384749	56.2 ± 7.8	10	high	5 μm × 5 μm

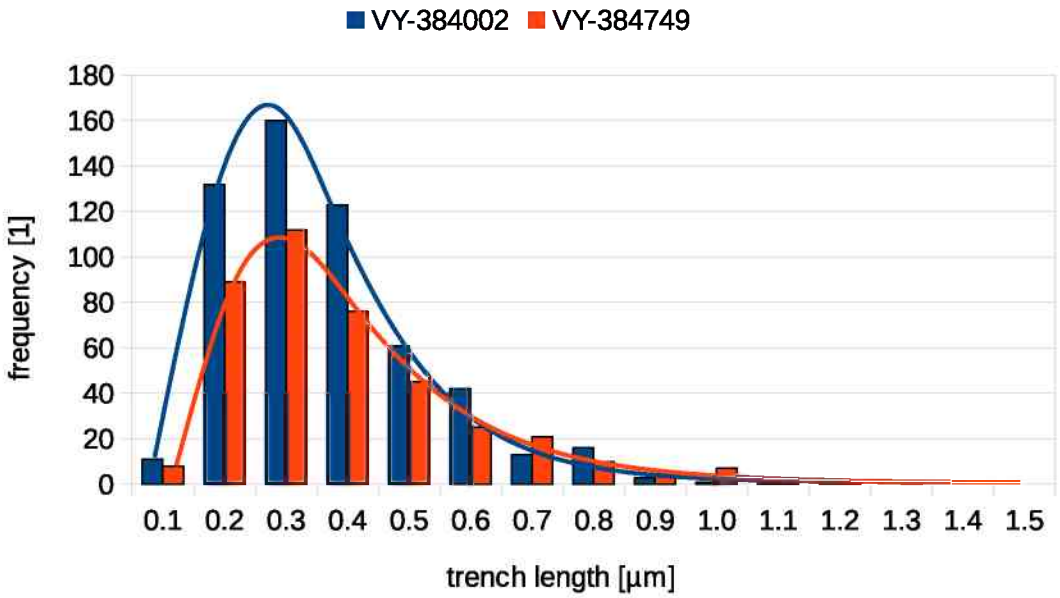

Figure 4.31: Histogram of the trench length distribution of set 2. The blue bars denote VY-384002 and the red bars denote VY-384749. The fits of the log-normal distribution are indicated by the solid lines.

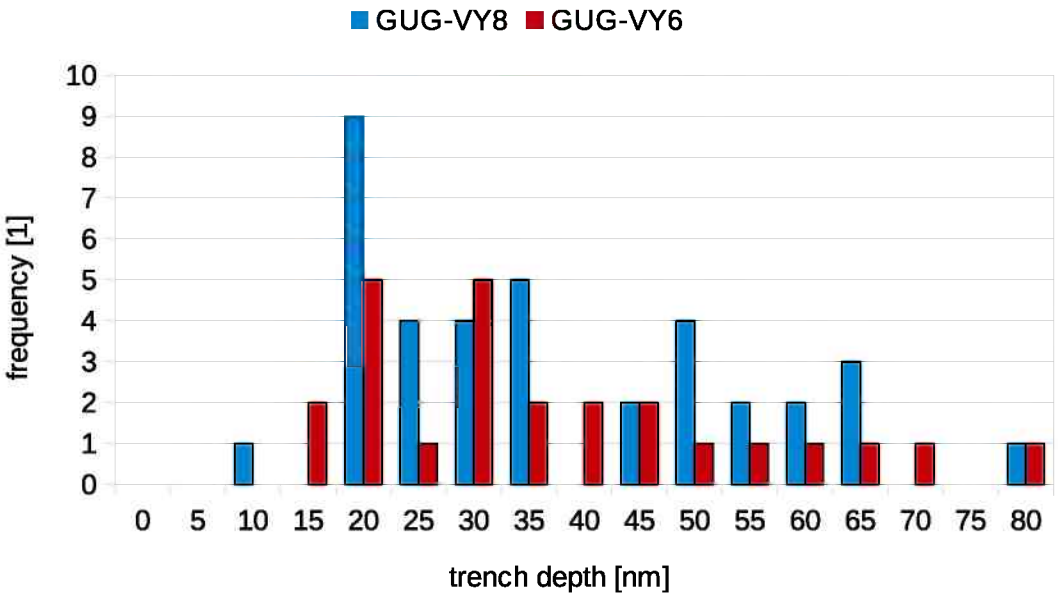

Figure 4.32: Histogram of the trench depth distribution of set 1. The blue bars denote GUG-VY8 and the red bars denote GUG-VY6.

5 Conclusions and Outlook

5.1 Conclusion

In this work, the sorption balance has been utilized as a tool for gravimetric, isothermal determination of water uptake from vapor on cellulosic fibers. It was possible to measure the water uptake of sample masses between 20 mg and 200 mg. In this context, Atomic Force Microscopy was presented as a technique to characterize the surfaces of isolated viscose fibers under ambient conditions. The analysis of the topography was aimed to draw connections between the fiber surface and water absorption. For this, the fibers were classified into fibers with water uptake above and below average.

After first trials in sorption measurements, a modification into two types of sample configurations were realized. They revealed two different forms of sorption isotherms. The viscose fibers of the 20 mg series, where the samples are loose fiber bundles of roughly 20 mg, resemble the *H4* hysteresis loop. The adsorption and desorption curves are mostly parallel and horizontally aligned. This shape of hysteresis loop is contributed to slit-like pores and plate-like agglomerations. This correlates to ripples, parallel to the main fiber axis, on the respective viscose fibers, presented in Fig. 3.2 of chapter 3. Furthermore, the regions in the sorption isotherms with high RH, where the influence of network effects, like capillary forces, have been expected, were rather unremarkable. The relative water uptake of the viscose fibers, provided by Kelheim Fibres, was for all samples slightly above 20 %. Only the pulp fiber samples displayed inferior capabilities of water uptake in both series. The form of the sorption isotherms of the wire cage series, where the fibers were packed tightly and compressed into a wire cage, show a closer resemblance to *H2* hysteresis loops. The isotherms exhibited saturation at high RH, indicating filled pore networks and bulk water on the fiber surfaces. The latter might be attributed to aforementioned network effects. The relative water uptake of the viscose fibers were all above 30 %. Thus, the results with the loose bundles of fibers are believed to approach isolated single fiber behavior, while the wire cage series correlates to fiber network behavior, similar to commercial products.

For AFM based topographical analysis, the industrial collaborator Kelheim Fibres provided two sets of trilobal viscose fibers, all called Galaxy. Each set consisted of fibers from batches with a water absorption capacity above and below average. Due to the curvature of the fibers, the recording of AFM images was limited to a scan size of 5 $\mu m \times 5\ \mu m$. In a comprehensive roughness analysis, the parameters σ, ξ, and α were obtained. Without regard for the curvature and surface impurities, all viscose fibers displayed a rather smooth surface with an RMS-roughness between 15 nm and 35 nm. Including aforementioned surface features, the average values for σ can increase

drastically, depending on the scan site. It was asserted that the influence of surface impurities is negligible. For set 2, with the batches VY-384002 and VY-384749, a correlation between RMS-roughness and water absorption was found. There, the batch with higher water absorption displayed a σ three times higher. This relation could not be confirmed for set 1, where the average RMS-roughness for both batches were identical. Thus, a general correlation between the RMS-roughness of viscose fibers and water absorption was not found. For the lateral correlation length and the Hurst parameter, slight trends regarding water absorption could be observed. In the case ξ, the deviations were too large and with α, the average values were too close to each other to proof a correlation to water absorption. The analysis of the surface morphology, aided by FFT analysis, found ripples, parallel to the main fiber axis, and trenches. The ripples vary in their distance to each other and are believed to be one of the factors contributing to the shape of aforementioned sorption isotherms of isolated single viscose fibers. The trenches were investigated by comparing the angle, length, depth, and density distributions of their respective batches. Only the trench density showed a trend, possibly correlating to water absorption. Therefore, the recording number of AFM images was increased and analyzed by an automated and less biased MATLAB script. The results indicated a correlation between a higher trench density and lower water absorption. For set 1, this result satisfied Welch's test for unequal variances with a significance level of 0.05. For set 2, this was true only at a significance level of 0.20. With this result, a correlation between trench density and water absorption remains ambiguous. In the end, among all investigated parameters, only the lateral correlation length and the trench density show possible correlation to the different water absorption capabilities of the samples.

5.2 Outlook

Based on the experience from this thesis, it is recommended to increase the number of recorded sorption isotherms for future investigations. Especially the wire cage series would benefit from this to verify the results obtained and outline the range of deviations. A characterization of the viscose fibers by small angle x-ray scattering (SAXS) would yield information about the fiber interior, especially the pore size and form. Ideally, a simultaneous application of the SAXS and the recording of a sorption isotherm would not only lead to a better understanding of the internal surface, but also about the in-situ pore filling.

For the AFM measurements, a further increase of AFM images for a statistical re-evaluation of the lateral correlation length ξ and the trench density is recommended, due to the great differences on the viscose fiber surfaces. For further improvements of the analysis methods, the MATLAB script for trench counting should be upgraded. The upgrades should implement improved mapping of the trenches, regarding the positions where a trench starts and where it ends. At this state, data of the trench angles and length would be viable byproducts. Another desirable upgrade would be regarding the bias of the operator. The script still depends on the manual input of

the thresholds. Furthermore, an investigation on a possible correlation between the mechanical properties and the water absorption capabilities of viscose fibers by AFM based nanoindentation (AFM-NI) was started [10,44,45]. This method yields information on the modulus and hardness of the investigated fibers and might lead to new insights regarding the understanding of water absorption of viscose fibers.

Acknowledgments

During the course of this work I met many people, whom I would like to thank

Ao. Univ.-Prof. Dr. Christian Teichert for being a kind and encouraging supervisor, for giving me the opportunity to work in the SPM Group and teaching me about AFM and surface science, for the chance to write this thesis and the correction of this work.

Dr. Christian Ganser for introducing me to the SPM Group, for teaching me AFM and showing me the ropes to everything related, for his excellent supervision, for his patience, his support and for being a good friend.

Ao. Univ.-Prof. Dr. Robert Schennach, Graz University of Technology, and head of the Christian Doppler Laboratory for "*Surface Chemical and Physical Fundamentals of Paper Strength*" for giving me the opportunity to be part in this, for the help, pointers, support, and discussions.

Univ.-Prof. Dr. Oskar Paris and **Dipl.-Ing. Roland. J. Morak** for giving me the opportunity to utilize the sorption balance, for discussions and for having an open ear regarding problems with the sorption balance.

Priv.-Doz. Dr. Beate Oswald-Tranta for her expertise and tremendous help with Matlab regarding the trench count algorythm.

Dr. Ingo Bernt and **Dr. Walter Roggenstein**, Kelheim Fibres, for providing the samples and stimulating discussions.

Dr. Markus Kratzer for discussions and lending an ear for all sorts of problems.

Dr. Franz J. Schmied, Dipl.-Ing. Leo Arpa, Dr. Wolfgang J. Fischer, Dr. Frederik Weber, Dr. Albrecht Miletzky, Dipl.-Ing. Sebastian Rohm, Dr. Ulrich Hirn, Dr. Rene Eckhart, Univ.-Prof. Dr. Wolfgang Bauer, Dr. Stefan Diebald, Dr. Jussi Lahti, Dipl.-Ing. Siegfried Zöhrer, Dipl.-Ing. Johannes Leitner and **Caterina Czibula** for the nice atmosphere within the CD-Lab and for helpful discussions.

Dipl.-Ing. Quan Shen, Jakob Genser, Dipl.-Ing. Stefan Klima, Dr. Andreas Nevosad, Michael Huszar, Michael Lasnik, Mgr. inz. Monika Mirkowska,

Dipl.-Ing. Stefan Lorbek, Lukas Kormos, MSc. Benjamin Kaufmann for providing a fun and nice work environment at the Institute of Physics.

Ing. Heinz Pirker for technical support.

Heide Kirchberger and **Magdalena Ottrin** for administrative support at the Institute of Physics.

Esther Schennach, MSc. for taking on plenty administrative tasks behind the curtains of the CD-Lab and her support.

Christian Doppler Research Society for financial support.

My family and **my friends** for their support, encouragement and sometimes for bearing with me.

Thank you.

Appendix A: Matlab trench count script

```
1
2  clear variables
3  close all
4
5  %% the method: duration ca. 5-30 seconds
6
7  %% Loading the text matrix
8
9  A=load('D:\Arbeit\Kreiml\rms_vy\120518\vy_384002_1_0007.txt');
10 figure; imshow(A*1e8, []); title('Original image');
11 impixelinfo;
12
13 % Turning the image into a greyscale image
14 A2=mat2gray(A*1e8);
15
16 % PARAMETERS
17 threshold = 3.0
18 impurity = 0.52
19
20
21 %% Background subtraction
22 [ny, nx] = size(A2);
23 [X,Y] = meshgrid([1:nx], [1:ny]);
24 xx=[X(:)'; Y(:)'];
25 sf = fit( xx', A2(:), 'poly22' );
26 Afit = sf( X(:), Y(:) );
27 Afit=reshape(Afit, ny,nx);
28 figure, imshow(Afit,[]);
29 A2=A2-Afit;
30
31 figure; imshow(A2, []); title('Cleaned image');
32 impixelinfo;
33
34
```

```
35 %% Normalization of the image and impurity detection + marking
36
37 A2=(A2-min(A2(:)))/(max(A2(:))-min(A2(:)));
38 A20=A2; % Backup of image for final presentation with overlap
39 [x,v] = imhist(A2);
40 figure; imshow(A2, []); title('Normalized image');
41 impixelinfo;
42 figure, plot(v, x);
43 D=im2bw(A2,impurity); % PARAMETER
44 SE = strel('diamond',6);
45 D=bwmorph(D,'dilate');
46
47 figure; imshow(D,[]);
48 ind=find(D==1);
49 defekt=ind; % Indices of impurities are saved
50
51
52 %% Calculation of the derivatives
53
54 [Bx,By]=gradient(A2);
55 % Y-direction chosen for better performance
56 By=By*1e4;
57 figure;
58
59 % Plots of derivatives in x-direction and y-direction
60 subplot(1,2,1);
61 imagesc(Bx); colormap 'gray';
62 title('Bx')
63 subplot(1,2,2)
64 imagesc(By); colormap 'gray';
65 title('By')
66
67
68 %% Histogram + plot
69
70 % The histogram helps at adjusting parameters
71 C=mat2gray(By);
72 figure;
73 imshow(C, []);
74 impixelinfo;
75 [x,v] = imhist(C);
76 figure, plot(v, x);
77
78
```

```
79 %% Edge detection
80
81 [bw, thres]=edge(C, 'canny');
82 bw =edge(C, 'canny', threshold*thres); % PARAMETER
83 figure, imshow(bw, []);
84
85 % Dilation
86 SE = strel('rectangle',[6 4]);
87 % modification of binary image (trenches)
88 % note: dependent on image resolution
89
90 bw = imdilate(bw,SE);
91 imshow(bw)
92
93 [L,num] = bwlabel(bw,4); % searching for connected areas (trenches)
94 figure, imshow(L,[]); colormap 'default';
95
96 % Loop for eliminating overlaps between impurities and trenches
97 for i=1:num
98     bDef=0;
99     ind0=find(L==i);
100    for j=1:numel(ind0)
101        if min(abs(defekt-ind0(j))) == 0
102            bDef =1;
103            break;
104        end
105    end
106    if bDef
107        bw(ind0)=0;
108    end
109 end
110 % Incidents with same indices leads to deletion of trench index
111
112 % Plot
113 figure, imshow(bw);
114
115 % Find connected components in binary image
116 cc = bwconncomp(bw, 8)
117
118
119 %% Presentation
120
121 % Backup image from before for presentation
122 % with trenches and impurities
```

```
123 C=A20;
124
125 % Marks the found edges on the image with red
126 ind=find(bw==1);
127 [n,m,z] = size(C);
128 plotPic = zeros( n,m,z,3);
129 picR = C;
130
131 picR(ind) = 1;
132 picR(defekt)=0; % Marks impurities
133 picG = C;
134 picG(ind) = 0;
135 picB = C;
136 picB(ind) = 0;
137
138 plotPic(:,:,:,1) = picR ;
139 plotPic(:,:,:,2) = picG ;
140 plotPic(:,:,:,3) = picB ;
141 A=plotPic(:,:,1,:);
142 A=reshape(A, n,m,3);
143 figure, imshow(A, []);
```

Bibliography

[1] Woodings, C. (2001) *Regenerated cellulose fibres*, vol. 18. Woodhead Publishing.

[2] Ibarra, D., Köpcke, V., and Ek, M. (2010) Behavior of different monocomponent endoglucanases on the accessibility and reactivity of dissolving-grade pulps for viscose process. *Enzyme Microb. Technol.*, **47**, 355–362.

[3] Klemm, D., Heublein, B., Fink, H., and Bohn, A. (2005) Cellulose: Fascinating Biopolymer and Sustainable Raw Material. *Angew. Chem. Int. Ed.*, **44**, 3358–3393.

[4] Rowell, R., Pettersen, R., Han, J., Rowell, J., and Tshabalala, M. (2005) Cell wall chemistry. *Handbook of wood chemistry and wood composites*, pp. 33–77, CRC Press, Boca Raton.

[5] Ganser, C. (2011) *Surface characterization of cellulose fibers by atomic force microscopy in liquid media and under ambient conditions*. Master's thesis, Montanuniversität Leoben.

[6] Krässig, H., Schurz, J., Steadman, R. G., Schliefer, K., and Albrecht, W. (2007) *Cellulose*, pp. 1–55. Wiley-VCH Verlag GmbH & Co. KGaA.

[7] Donaldson, L. (2007) Cellulose microfibril aggregates and their size variation with cell wall type. *Wood Sci. Technol.*, **41**, 443–460.

[8] Booker, R. and Sell, J. (1998) The nanostructure of the cell wall of softwoods and its functions in a living tree. *Holz Roh- Werkst.*, **56**, 1–8.

[9] Terashima, N., Kitano, K., Kojima, M., Yoshida, M., Yamamoto, H., and Westermark, U. (2009) Nanostructural assembly of cellulose, hemicellulose, and lignin in the middle layer of secondary wall of ginkgo tracheid. *J. Wood Sci.*, **55**, 409–416.

[10] Ganser, C. (2014) *Influence of water on mechanical properties of cellulosic materials studied by AFM based methods*. Ph.D. thesis, Montanuniversität Leoben.

[11] Schmied, F. J., Teichert, C., Kappel, L., Hirn, U., Bauer, W., and Schennach, R. (2013) What holds paper together: Nanometre scale exploration of bonding between paper fibres. *Sci. Rep.*, **3**, 2432.

[12] Harms, H. (2003) Lenzing LYOCELL: Potentiale und Chancen einer neuen Fasergeneration. *Materialwissenschaft und Werkstofftechnik*, **34**, 267–271.

[13] Harms, H. (2008), Fasertechnologie. Vorlesungsskriptum an der Montanuniversität Leoben.

[14] Smole, M. S., Peršin, Z., Kreže, T., Kleinschek, K. S., Ribitsch, V., and Neumayer, S. (2003) X-ray study of pre-treated regenerated cellulose fibres. *Mater. Res. Innovations*, **7**, 275–282.

[15] Lenz, J., Schurz, J., and Wrentschur, E. (1988) The fibrillar structure of cellulosic man-made fibers spun from different solvent systems. *J. Appl. Polym. Sci.*, **35**, 1987–2000.

[16] https://www.ipz.tugraz.at/index.php/wbPage/wbShow/coimage/Unbenannt.jpg (2016). TU Graz.

[17] http://impulse2013.bayern-innovativ.de/249e13d5-7f84-f37e-1fed-3a16391d1127 (2016). Bayern-innovativ.

[18] Sensirion AG (2014), Introduction to humidity - basic principles on physics of water vapor. Application Note.

[19] Sing, K. S. (1985) Reporting physisorption data for gas/solid systems with special reference to the determination of surface area and porosity (recommendations 1984). *Pure and applied chemistry*, **57**, 603–619.

[20] Rigby, S. P. and Fletcher, R. S. (2004) Experimental evidence for pore blocking as the mechanism for nitrogen sorption hysteresis in a mesoporous material. *The Journal of Physical Chemistry B*, **108**, 4690–4695.

[21] Morishige, K., Tateishi, M., Hirose, F., and Aramaki, K. (2006) Change in desorption mechanism from pore blocking to cavitation with temperature for nitrogen in ordered silica with cagelike pores. *Langmuir*, **22**, 9220–9224.

[22] Erko, M. (2012) *Water properties in confined geometry*. Ph.D. thesis, Montanuniversität Leoben.

[23] Sarkisov, L. and Monson, P. A. (2001) Lattice model of adsorption in disordered porous materials: Mean-field density functional theory and monte carlo simulations. *Physical Review E*, **65**, 011202.

[24] Ravikovitch, P., Domhnaill, S. Ó., Neimark, A., Schüth, F., and Unger, K. (1995) Capillary hysteresis in nanopores: theoretical and experimental studies of nitrogen adsorption on mcm-41. *Langmuir*, **11**, 4765–4772.

[25] Binnig, G., Quate, C., and Gerber, C. (1986) Atomic force microscope. *Phys. Rev. Lett.*, **56**, 930–933.

[26] Morita, S., Wiesendanger, R., and Meyer, E. (2002) *Noncontact atomic force microscopy*, vol. 1. Springer, Berlin.

[27] Zhong, Q., Inniss, D., Kjoller, K., and Elings, V. (1993) Fractured polymer/silica fiber surface studied by tapping mode atomic force microscopy. *Surf. Sci. Lett.*, **290**, L688–L692.

[28] Nečas, D. and Klapetek, P. (2012) Gwyddion: an open-source software for SPM data analysis. *Cent. Eur. J. Phys.*, **10**, 181–188.

[29] Hosemann, P. (2004) *Characterization of cellulose fibers using Atomic-Force Microscopy*. Master's thesis, Montanuniversität Leoben.

[30] Schmied, F. J. (2008) *Characterization of cellulose type I and type II fibers using Atomic-Force Microscopy*. Master's thesis, Montanuniversität Leoben.

[31] Schmied, F. J. (2011) *Atomic Force Microscopy investigations of fiber-fiber bonds in paper*. Ph.D. thesis, Montanuniversität Leoben.

[32] Schrödl, N., Bucher, E., Egger, A., Kreiml, P., Teichert, C., Höschen, T., and Sitte, W. (2015) Long-term stability of the IT-SOFC cathode materials La 0.6 Sr 0.4 CoO 3 - δ and La 2 NiO 4 + δ against combined chromium and silicon poisoning. *Solid State Ionics*, **276**, 62–71.

[33] Teichert, C. (2002) Self-organization of nanostructures in semiconductor heteroepitaxy. *Phys. Rep.*, **365**, 335–432.

[34] Zhao, Y., Wang, G., and Lu, T. (2001) *Characterization of amorphous and crystalline rough surface: principles and applications*. Academic Press, San Diego.

[35] Cooley, J. and Tukey, J. (1965) An algorithm for the machine calculation of complex Fourier series. *Math. Comput*, **19**, 297–301.

[36] Frigo, M. and Johnson, S. (2005) The design and implementation of FFTW3. *Proc. IEEE*, **93**, 216–231.

[37] http://www.kelheim fibres.com/ (2016). Kelheim Fibres.

[38] MATLAB (2010) *version 7.10.0 (R2010a)*. The MathWorks Inc.

[39] Morak, R. (2013) *Structure and sorption analysis of wood templated ceramics*. Master's thesis, Montanuniversität Leoben.

[40] Jähnert, S. (2008) *Study of pure substances in periodic mesoporous silica material with thermophysical methods and in-situ small-angle x-ray-diffraction*. Ph.D. thesis, Dissertation Technische Universität Berlin.

[41] Groß, S. and Findenegg, G. H. (1997) Pore condensation in novel highly ordered mesoporous silica. *Berichte der Bunsengesellschaft für physikalische Chemie*, **101**, 1726–1730.

[42] Ibbett, R., Kaenthong, S., Phillips, D., and Wilding, M. (2006) Characterisation of the porosity of regenerated cellulosic fibres using classical dye adsorption techniques. *Lenzinger Berichte*, **85**, 77–86.

[43] Welch, B. (1947) The generalization of student's problem when several different population variances are involved. *Biometrika*, **34**, 28–35.

[44] Ganser, C., Kreiml, P., Morak, R., Weber, F., Paris, O., Schennach, R., and Teichert, C. (2015) The effects of water uptake on mechanical properties of viscose fibers. *Cellulose*, pp. 1–10.

[45] Ganser, C., Hirn, U., Rohm, S., Schennach, R., and Teichert, C. (2014) AFM nanoindentation of pulp fibers and thin cellulose films at varying relative humidity. *Holzforschung*, **68**, 53–60.